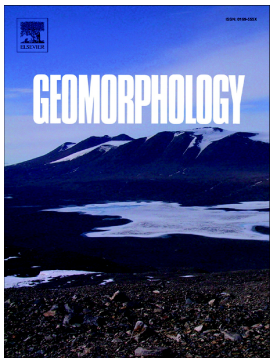

Digital landform reconstruction using old and recent open access digital aerial photos

Adrián Riquelme, Matteo Del Soldato, Roberto Tomás, Miguel Cano, Luis Jordá, Sandro Moretti

PII: S0169-555X(19)30003-0
DOI: https://doi.org/10.1016/j.geomorph.2019.01.003
Reference: GEOMOR 6637

To appear in: *Geomorphology*

Received date: 30 January 2017
Revised date: 30 October 2018
Accepted date: 4 January 2019

Please cite this article as: Adrián Riquelme, Matteo Del Soldato, Roberto Tomás, Miguel Cano, Luis Jordá, Sandro Moretti , Digital landform reconstruction using old and recent open access digital aerial photos. Geomor (2019), https://doi.org/10.1016/j.geomorph.2019.01.003

Digital landform reconstruction using old and recent open access digital aerial photos

Adrián Riquelme[a]*, Matteo Del Soldato[a, b,c], Roberto Tomás[a], Miguel Cano[a], Luis Jordá[d] and Sandro Moretti[c]

a Department of Civil Engineering, University of Alicante P.O. Box 99, E-03080 Alicante, Spain

b Department of Earth Sciences, Environment and Resources, Federico II University of Napoli, Largo San Marcellino 10, 80138 Naples, Italy.

c Department of Earth Sciences, University of Firenze, Via La Pira 4, 50121 Florence, Italy

d Geological Survey of Spain, Ríos Rosas 23, 28003 , Madrid, Spain

*Corresponding author: Adrián Riquelme, Department of Civil Engineering, University of Alicante, Spain. ariquelme@ua.es

Abstract

Technological progress in remote sensing has enabled digital representation of terrain through new techniques (e.g. digital photogrammetry) and instruments (e.g. 3D laser scanners). However, the use of old aerial images remains important in geosciences to reconstruct past landforms and detect long-term topographic changes. Administrations have recently expressed growing interest in sharing photogrammetric datasets on public repositories, providing opportunities to exploit these resources and detect natural and anthropogenic topographic changes. The SfM-MVS photogrammetric technique was applied to scanned historical black and white aerial photos of the Serra de Fontcalent (Alicante, Spain), as well as to recent high-quality digital aerial photos. Ground control points (GCPs) extracted from a LiDAR-derived three-dimensional point cloud were used to georeference the results with non-linear deformations. Two point clouds obtained with SfM-MVS were compared with the LiDAR-derived reference point cloud. Based on the result, the quality of the models was analysed through the comparison of the stages on stable areas, i.e., lands where no variations were detected, and active areas, with quarries, new infrastructures, fillings, excavations or new buildings. This study also indicates that errors are higher for old aerial photos (up to 5 m on average) than recent digital photos (up to 0.5 m). The application of SfM-MVS to open access data generated 3D models that enhance the geomorphological analysis, compared to stereophotogrammetry, and effectively detected activities in quarries and building of landfills.

***Keywords**: SfM, aerial photos, anthropogenic change detection, 3D reconstruction*

1 Introduction

In recent years, innovations in remote sensing techniques have increased the potential to measure ground surfaces and their changes. The spatial resolution of measurements has significantly improved with the introduction of the Global Positioning System (GPS) (Brasington et al. 2000; Brückl et al. 2006), Remotely Piloted Aircraft Systems (RPAS)

(Niethammer et al. 2012) and airborne and terrestrial laser scanning (Razak et al. 2011). These methods provide digital elevation models (DEMs) that are useful for geomorphological analyses. Stereo aerial photos provide three-dimensional scenes for the overlapped area of two images. The application of stereophotogrammetry to historical aerial photos has enabled the observation of geomorphological changes throughout decades (Chandler and Moore 1989; Chandler and Brunsden 1995; Su and Stohr 2000; Hapke 2005). Stereoscopes underexploit the potential of images, and nowadays several free and commercial software packages enable 3D vision (through anaglyph glasses). 3D computer vision algorithms have been considerably improved in the last decades and are the most important irruption of deep learning in visual recognition (Krizhevsky et al. 2012), e.g. Visual SLAM (Engel et al. 2014; Engel et al. 2017).

Structure-from-Motion (SfM) is a relatively new photogrammetric method that emerged in the late 1970s (Ullman 1979). SfM can be applied to the geomorphological analysis of landforms and their evolution by means of 3D models (Snavely et al. 2008; Westoby et al. 2012; Eltner et al. 2016). SfM uses a number of digital images (Gomez et al. 2015) and automatically solves the geometry of the scene and camera position and orientation by means of an iterative bundle adjustment procedure (Snavely et al. 2008). SfM, along with multi-view stereo (MVS) algorithms, enables the generation of dense 3D point clouds (3DPC) from a set of digital photos (Hartley and Zisserman 2003; Szeliski 2010; Fisher et al. 2013). Existing SfM-MVS software packages, such as Visual SfM (Wu et al. 2011; Wu 2011; Wu 2013), apply methods such as Cluster Multiview Stereo (CMVS) and Patch based Multi-View Stereo (PMVS). However, the employed methods are not revealed for some packages, such as Agisoft Photoscan (Agisoft LLC 2016a). The use of Ground Control Points (GCPs) and known object-space coordinates enables the projection of the photogrammetric results to a system of absolute coordinates. Then the generated 3DPC can be applied to geoscientific studies.

3D laser scanning facilitates the acquisition of a 3DPC, which registers a surface in a specific moment. However, a major issue with these types of applications is the impossibility of obtaining past digital information (Ishiguro et al. 2016). Contrarily, the SfM-MVS technique reconstructs a surface by means of digital non-metric photos. James and Robson (2012) concluded that "[…] SfM-MVS approach can produce surface or topographic data over scales and stages relevant to a broad range of geoscience applications". Therefore, if digital photos of a past stage are available, it is reasonable to consider the generation of DEMs for past times.

Difficulties arise, however, when attempting to use SfM-MVS with non-digital datasets. Despite the existence of several digital landscape photos made available by governments, regional and local agencies, sometimes images were not captured following practical flight plans for SfM-MVS (James and Robson 2014). The main limitation of using these old photos is the small overlap between contiguous photos: the number of captures of a single feature on the surface could range between 2 and 6 when using historical photos. As SfM-MVS usually requires a high overlap degree, old aerial

photos may not be appropriate for the application of SfM-MVS. However, a recent study has obtained good results using only three aerial oblique images to generate DEMs with SfM-MVS (Midgley and Tonkin 2017).

As the SfM-MVS method is only limited by the camera resolution (James and Robson 2012), the application of historical aerial photos to the landform reconstruction (e.g. mountains, glaciers, landslides, volcanoes, etc.) can provide useful information to geomorphologists. Previous studies have reported on the application of non-digital historical aerial photos to the diachronic reconstruction of geomorphological landform evolution and vegetation investigations (Gomez et al. 2015) and to active volcanic areas (Gomez 2014; Ishiguro et al. 2016). Other studies have highlighted the potential of historical aerial images for glaciological monitoring through the production of DEMs (Barrand et al. 2009; Kjeldsen et al. 2015; Midgley and Tonkin 2017). Moreover, UAV-derived aerial imagery has been used to monitor environmental changes in glaciers (Tonkin et al. 2016), to produce digital surface models (DSMs) of moraines (Tonkin et al. 2014) and to detect erosion in river channels (Cook 2017). There have been several recent attempts to evaluate DSMs from multitemporal aerial photos using SfM-MVS. The surveys conducted by Ishiguro (2016) demonstrated that the use of GCPs acquired by global navigation satellite systems (GNSS) and levelling surveys can generate DEMs with accuracies comparable to those of conventional photogrammetry. The study of Hsieh et al (2016) reported on the application of aerial photogrammetry along with ALS and RPAS techniques to analyse landslides. Also, researchers have recently examined the ability to generate shallow-water bathymetry using SfM-MVS (Purdie et al. 2016).

When using aerial photos with SfM-MVS, a major issue that has already been highlighted is the accuracy level of the reconstructed models. Therefore, accuracy must be assessed by comparing the aerial photos to a reliable benchmark. For instance, Gomez et al (2015) generated DEMs using black-and-white and colour aerial photos and GPS control-points and compared these to an official DEM provided by the Geospatial Information Authority of Japan (GSI). Gomez et al (2015) assessed the accuracy of those DEMs, establishing a linear regression with a 0.965 squared correlation coefficient (R^2). Ishiguro et al (2016) evaluated the accuracy of DSMs generated from archived aerial photos and verified that their models could measure altitude with a 121.5 cm root-mean-square-error (RMSE). Tonkin et al (2016) generated a DEM of a glacier (using five aerial images from 2003 and only three GCPs) and compared it with a LiDAR-derived 3DPC. The comparison showed a 0.888 m RMSE (σ=0.812 m), and interestingly, residuals appeared to be spatially distributed and increasing in areas subject to poor ground control. Later, Midgley and Tonkin (2017) reconstructed a glacier using 1936 oblique aerial photos and compared them with LiDAR data, finding a mean vertical difference of 0.5 m (σ=8.5 m and RMSE=8.5 m) in stable areas.

Although the study presented herein did not use the SfM-MVS method, but photogrammetric methods, preliminary work on the number of GCPs was also undertaken by Barrand et al. (2009), where a 6 km^2 glacier surface was reconstructed, using historical aerial images and different LiDAR-derived GCP configurations. An increase in the number

of GCPs resulted in a lower root-mean-square (RMS) error of adjusted GCP positions, and the utilisation of 20-25 GCPs provided good results. Barrand et al. (2009) also highlighted that while LiDAR data density varied according to scan height above the surface, topography and the presence of swath overlaps, the spatial resolution of the dataset was estimated at approximately 1.15 pts m^{-2}. Recent studies have reported that at least 10 - 15 GCPs, distributed evenly within the area of interest, are necessary to provide good georeferencing (Gomez et al. 2015; Agisoft LLC 2016b). However, not only the quantity of GPCs affects the results, but its distribution is also a key factor. An interesting recent study conducted by Tonkin and Midgley (2016) has shown that DSM quality is improved when four or more GCPs (up to 101 were studied) are used. Moreover, Tonkin and Midgley (2016) also investigated the influence of GCP distribution, finding that the vertical error increased with distance from the GCPs cluster.

Concerning the source of the GCPs, preliminary work was undertaken by several researchers. Different sources of information were used: Global Navigation Satellite Systems (GNSS) (Gomez et al., 2015), levelling points (Ishiguro et al., 2016), Google Earth software (Kropáček et al., 2015), and ALS-derived point clouds (Barrand et al., 2009; Hsieh et al., 2016; Midgley and Tonkin, 2017).

Published studies use recently acquired photos to conduct the reconstruction of the landform. However, few studies focus on the use of existing aerial photos, originally intended to be used with stereophotogrammetry. Herein the potential use of historical aerial photos to reconstruct landforms is explored, along with the potential of monitoring the evolution of landform with these DEMs. The landform of the Sierra de Fontcalent (Alicante, Spain) is studied with three different sources of information: a set of printed black and white aerial photos, an airborne laser scanner (ALS) point cloud and a set of digital colour photos. Accordingly, three stages are generated, corresponding to the years 1993, 2009 and 2014, respectively.

The generated models provide useful digital information for geomorphologists, enabling the analysis of morphological features of the landform at past stages. However, the accuracy of these models must be evaluated. The generated landforms were compared to the ALS-derived point cloud (benchmark). Active areas were analysed to verify the possibility of monitoring long-term unstable areas with the generated DEMs. This process enabled the identification of changes, along with their quantification. Accordingly, the comparison of the generated DEMs focused on: (1) stable areas, assessing how similar the generated model is to the benchmark, and (2) active areas (quarries, landfills, constructions, etc.), evaluating the error when calculating large- and small-scale changes on the surface.

The main objectives of the work presented herein are: (1) to demonstrate the ability of generating SfM-MVS derived DEMs from black-and-white historical non-digital and recently acquired high-resolution digital aerial nadir photos, using only public domain datasets when no fieldwork is possible (i.e. GPS, RPAS, etc.), and (2) to evaluate the capability of

these generated DEMs to detect and quantify changes. For reproducibility purposes, all data used herein is open-access, provided by the Spanish Government and available in public repositories.

2 Materials and Methods

2.1 Site description

A case study located in SE Spain (Fig. 1) was considered, where important anthropogenic changes associated with different activities have occurred throughout the last decades. The study area is located near the Mediterranean coast of Alicante, where rainfall is scarce, irregular and random. The summer drought extends from three to five months, with few rainy days. At the end of this period, heavy autumnal downpours cause numerous flooding episodes. The annual average temperature is 18.3°C and there is practically no meteorological winter. Potential evapotranspiration is high, with a 896 mm Thornthwaite index, which indicates a strong water deficit during most of the year (INGEMISA and Aurenheimer 1991). This climatic feature plus sparse vegetation (limited to small shrubs and small pine trees) increases the possibilities of the formation of ravines. The site presents a naked ground surface with scarce vegetation, favouring the extraction and insertion of GCPs. This work utilized publicly available aerial photos of the site corresponding to two past stages, which were captured in 1993 and 2014, and an ALS-derived 3DPC, which was scanned in 2009.

The area is located within a highly tectonized context, where Keuper facies (Triassic period) played a key role, in association with the main fractures of the study area. The reliefs that stand out in the landform (i.e. Serra de Fontcalent, Serra Mediana, and Serreta Llarga) correspond to the mountains with most resistant carbonate lithologies (limestones and dolomites). The areas with softer relief, often formed by endorheic zones, present marly lithologies and Keuper facies (gypsum and marls) (Fig. 2).

In the Foncalent Mountain, carbonate materials that represent the complete Jurassic series outcropping are present: dolomitic and oolitic limestones (Lower Jurassic), micrithic limestones with flint nodules (Middle Jurassic), nodular marly limestones of Ammonitic Rosso facies (Upper Oxfordian) and bedded micrithic limestone (Tithonian). A karstic-type erosive model, which generates marked escarpments, affects harder calcareous material (limestones and dolomites). These exhibit pronounced structural control, following fault lines, where the Jurassic materials are against Cretaceous materials. Detrital marls and marly limestones of the Cretaceous occupy the mountainside of Sierra de Fontcalent and lower locations, where ravine formation processes reach maximum development, constituting the substrate on which the glacis of the sector developed. The Sierra de Fontcalent environment holds a set of glacis that corresponds to old forms that are not in equilibrium with current climatic conditions. One of the most developed glacis corresponds to the SE side of this mountain, where caliche developed, covering the surface of the glacis, including pebbles from the slope crown that "fossilize" the union with the piedmont.

Almost the entire study area remained stable during the last decades. In this work, stable areas were used to assess the accuracy of the reconstructed models. Several subsectors that have suffered anthropic-originated changes from 1993 to 2014 were used to test the possibility of monitoring the evolution of the landform. The unstable areas present a variety of extensions and heights. Two industrial estates are located southeast to the sector: Las Atalayas and Pla de la Vallonga. Changes in this subsector have 10 m order of magnitude. In the middle of the study area, three mountains can be found: Sierra de Fontcalent (south), Serra Mitjana (north) and Serreta Llarga (east). On the northeast side of Sierra de Fontcalent, there is a quarry that was active throughout the entire study period. The second mountain is Serra Mitjana, where an active quarry can be found on the East side. Finally, the third mountain is Serreta Llarga, which contains an inactive quarry (minerals for cement production). On the south side of Serra Mitjana, there is an urban solid waste landfill for the city of Alicante. This landfill was active during the entire analysis period. The order of magnitude of the changes in these quarries and waste treatment plant is 100 m. The AP7 highway (Autopista Mediterránea), which was built during 2004- 2007, crosses the west side of Serra Mitjana. The high-speed Alicante-Madrid railway was inaugurated in 2013 (construction began in 2009). The highway and the railway present changes with an order of magnitude of 1000 m in length and 10 m in height and width. Six subsectors were defined to analyse the generated DEMs in detail (Fig. 1b): (1) AP-7 highway, (2) solid waste treatment plant landfill, (3) industrial estate, (4) Serra Llarga, (5) Serra Mitjana and (6) Serra de Fontcalent.

2.2 Reconstruction of the landform at different stages

Since 1945, several acquisition campaigns have been carried out in SE Spain, during which aerial nadir images were captured. Due to the availability of aerial photos, the year 1993 was selected (October 1993 campaign by Generalitat Valenciana). The camera used was a WILD RC10 15UAG 1052 (focal length 153.26 mm), and the obtained images were printed in a 1/25.000 scale at 23x23 cm (Generalitat Valenciana 1993a). The calibration report for this camera showed that symmetric radial distortion, decentring distortion, and calibrated principal point were almost null (U.S. Geological Survey 2000).

This first stage consists of a set of non-digital black and white aerial photos, with corresponding numbers 5683-5686 and 5741-5745 (Generalitat Valenciana 1993b). The digitised photos are found on the Terrasit web service (Generalitat Valenciana 2016). Printed photos are also available at the Library of the University of Alicante, which were scanned at 600 dpi resolution. All digitised images were cropped to maintain the optical axis centred, removing fiducial markers and maintaining the same size: 4724 x 4724 px.

The second stage consists of a 3DPC, which was scanned using an ALS and coloured using the orthophotos provided by the “Plan Nacional de Ortofoto Aérea” (PNOA) project (Fig. 1 (b)). The aerial flight was performed in 2009, but unfortunately, the acquisition date of photos is not provided. The open access digital information is available in LAZ format, and each file represents an extension of 2x2 km. This point cloud has a density of 0.5 pts m^{-2} and an accuracy of

20 cm in height. The point cloud is georeferenced in the ETRS-89 (30N) geodetic system and all elevations are orthometric (Instituto Geográfico Nacional de España 2016).

The third stage consists of a set of digital aerial photos captured in 2014, provided by the PNOA project. All images are freely available in ECW format (Instituto Geográfico Nacional 2016). Photos were taken by the company Servicios Politécnicos Aéreos S.A., with an UltraCam X (Serial Number UCX-SX-1-50013345) manufactured by Vexcel Imaging GmbH. The field calibration report of this camera indicated that it does not require any calibration update (Vexcel Imaging 2014). The pixel size is 0.22 metres, 8 bits, and dimensions of photos vary between 9419x14429 and 9420x14430 px.

2.3 Landform reconstruction

The first step (stage 1 in Fig. 3) considered the availability and quality of aerial photos. This stage focused on the use of existing non-digital black and white aerial photos, which were digitised by a scanner. Herein, only readily available instruments were utilised, which included a Ricoh MP500 scanner with 600 dpi resolution. This scanning process was not required when digital images were used. Scanned images were then cropped preserving the centre pixel coincident with the intersection of the optical axis and the surface (Stage 2 in Fig. 3), masking the fiducial markers from processing. All cropped photos had the same pixel size so that the SfM-MSV software processed all photos with the same parameters.

The alignment process estimated internal and external camera orientation parameters in the local "image-space" coordinate system and correlated the images to each other (Stage 2 in Fig. 3). During this process, the model was linearly transformed (several parameters transformed), undergoing translation, rotation, and escalation. The SfM-MVS method was used to align the images. This step provided a sparse point cloud along with the relative position and orientation of the aerial photos.

When accurate GCPs are not available, public DEMs provided by governments and digital information are interesting alternatives. In Spain, the PNOA project (Instituto Geográfico Nacional de España 2016) provides geo-referenced models of the terrain, and therefore GCPs were extracted from an ALS-derived point cloud. This 3DPC presents 20 cm elevation accuracy and point density of approximately 0.4 pts/m^2. Consequently, features could only be roughly identified (for example, crossroads, trees, rocks or building roofs). This 3DPC was used as a benchmark. The ALS-derived point cloud had outliers, which were removed by the Statistical Outlier Removal (SOR) filter (Rusu et al. 2008) from CloudCompare (Girardeau-Montaut 2016). The parameters utilised were 10 neighbours with a 5σ standard deviation, where σ is the standard deviation of the distances between the selected point and its corresponding 10 nearest neighbours.

The GCPs and tie points (i.e. GPCs with no coordinates) were inserted to optimise the parameters of the camera and to georeference the reconstruction. An iterative process (Fig. 3) followed herein, in which the intermediate result was improved by inserting more GCPs and tie points, and optimising again. The number of inserted GCPs for the first and third stage was 150 and 294, respectively. In both cases, GCPs were evenly distributed and their locations were selected

on the basis of visual inspection between digitised photos and the reference 3DPC. Firstly, GCPs were inserted into stage 1, which was by far the most difficult stage in terms of feature identification because of pixel size and greyscale colourings. Secondly, all existing GCPs in stage 1 were identified in stage 3. Although most GCPs were successfully identified, changes in landform (vegetation, changes in land use and other human activities) prevented the identification of some GCPs and therefore, additional GCPs were inserted. During GCP insertion and 3DPC generation, the convenience and necessity of including more GCPs in steep areas of Sierra de Fontcalent and Sierra Mitjana was confirmed. Overall, 21 tie points were included to improve the reconstruction process.

After the addition of GCPs, camera parameters were optimised and the error of each GCP was automatically calculated in metres and in pixels. Those points with unacceptable errors (e.g., 10 m) were revised, followed by correction of position or removal. Self-calibrating bundle adjustment enabled calibration of internal parameters. Focal length (f) was 3571.96 px for stage 1 and 13916.2 px for stage 3. Principal point coordinates were also calibrated for the first stage because scanned images were manually cropped, resulting in c_x and c_y equal to -16.9384 and -48.7693 px, respectively. Table 1 shows the residual mean square errors of the GCPs used in both stages. Table A.1 shows the processing parameters of the SfM-MVS process and summarizes the results for stages 1 and 3. In Table A.1, the reprojection error is the distance between the point on the image where a reconstructed 3D point can be projected and the original projection of that 3D point detected on the photo and used as the basis for the 3D point reconstruction procedure (Agisoft LLC 2016a).

Fig. 4 shows how the photos overlap in both stages; the specific flight plan resulted in that captured photos only overlapped with their precedent and following photos within the same line. Fig. 4a also shows that the overlap between neighbouring flight lines is almost non-existent. Photos for the third stage presented more overlapping, and photos not only overlapped with their neighbouring captures but also with contiguous flight lines. Moreover, Fig. 4a also shows that in the 1993 stage, most of the points are present in two photos. However, in the 2014 stage, most of the points are present in 3 to 5 photos.

The software estimated camera positions and calculated depth information for each camera, generating a dense cloud with the MVS algorithm, and providing a dense cloud of the terrain surface. As an example of this, Fig. 5 presents the result of the calculation of the position and orientation of photos for stage 3. Once the point cloud was generated, reconstruction was visually inspected to detect empty areas or significant errors. Some areas required the addition of more GCPs or tie points for a better surface generation. If necessary, the previous step was repeated following an iterative process.

2.4 Model comparison and estimation of volumes.

The reconstructed surface for each stage was compared to the benchmark (Stage 3 in Fig. 1), which was the ALS-derived point cloud from which the GCPs were acquired. Therefore both models were defined based on the same reference system.

Two methods were initially considered to compare the generated DEMs. The first method was the rasterization of the DEM into a 2.5D model and comparison of height elevations. The second method was the Multiscale Model to Model Cloud Comparison (M3C2), which computes the local distance between two point clouds along the normal surface direction, tracking 3D variations in surface orientation (Brodu and Lague 2012; Lague et al. 2013). The first method decimates the 3DPC, reducing the resolution of the results, but computation is simple and fast. The second method can work with a decimate point cloud or with the original point cloud and is particularly effective for steep slopes. Although the application of the M3C2 method could provide successful results, the 2.5D comparison method was employed herein due to its simplicity and speed.

Model generation not only enabled the comparison of the distances between the corresponding stages but also established the volumes; four different areas are compared to a reference plane herein. The estimated volumes of the selected areas presented different orders of magnitude. Additionally, other areas where no changes were expected (i.e. no differences in the volumes measured between stages) were selected. The measured volume provided information on the reliability and error when measuring volumes in similar conditions.

Volumes were measured with respect to an arbitrary horizontal reference plane, located at the minimum elevation of the reference stage. All volumes were calculated using the 2.5D volume calculation tool available in the CloudCompare software (Girardeau-Montaut 2016).

3 Results

3.1 DEMs of stages 1 and 3.

Fig. 6 presents an orthographic top view of the reconstructed landforms corresponding to stages 1 and 3, and the downloaded ALS-derived point cloud (stage 2). Cloud to cloud comparison

3.1.1 AP-7 highway

Relative height distances between 1993 and 2009 for each point of a 2.5 m grid are shown in Fig. 7d. A linear area is observed where surface elevation (yellow and red) and descent (blue) have occurred. This elevation change corresponds to the construction of the AP-7 highway and results in a significant topographical change. In the upper part of Fig. 7d, the blue areas correspond to areas of soil extraction, while yellow and red areas represent landfills. The remaining surface

shows variations close to zero (the green colour covers most of the surface), which means that the terrain relatively fits both stages.

The distances computed between stages 2 and 3 (2009-2014) are shown in Fig. 7e. As most of the surface is depicted in green, both stages present a good correspondence in terms of elevations. The AP-7 highway was built before 2009 and no change is expected to be detected between 2009 and 2014. Nevertheless, on the left side of the highway, an area that suffered a positive change (yellow) is identified, and visual inspection revealed that this area, next to the bridge, corresponds to a landfill. The time-lapse tool of Google Earth software shows that, in this area, the ground level was raised in 2012.

3.1.2 Solid waste treatment plant landfill

The elevation changes between stages 1 and 2 and between stages 2 and 3 are shown in Figs. 8d and 8e, respectively. Fig. 8d shows landfills on the left and right sides of the figure (yellow and red). In the central part of the figure, a blue area is identified, which corresponds to the excavation of a new landfill cell. Comparison of stages 2 and 3 shows that most of the surface is coloured in dark green, and the mean of distance distribution is almost zero. In other words, the generated model of stage 3 fits to stage 2 much better than the model generated for stage 1 (Fig. 8e). Fig. 8e shows that there has been a landfill to the right of the solid waste treatment plant (yellow and red) and that excavation works continued after 2009 (blue).

At this area, the surface suffers positive and negative variations, and a topographic transect has been extracted (Fig. 8f), which showed that from 0 to 300 m, distances between stages are under 1 m in the stable area. The transect also shows topographical changes between the studied stages and enabled the identification and quantification of the solid waste treatment plant (cell excavation and landfill). In those areas considered as “stable”, height difference was under 2 m.

3.1.3 Industrial estate

The elevation changes between stages 1 and 2 and between stages 2 and 3 are shown in Figs. 9d and 9e, respectively. Fig. 9d refers to distances measured between stages 1 and 2 and shows a wide area, where no changes are expected, coloured in green, yellow and light blue. Fig. 9a shows that in the first stage (1993), the industrial estate Las Atalayas (SW) had recently been urbanised but few buildings had been built. Fig. 9d shows a pattern of rectangles coloured in red, which correspond to industrial buildings that were built between 1993 and 2009. The industrial estate Pla de la Vallonga (northeast), however, was fully active throughout the study period as most of the estates were already present. The comparison between stages 2 and 3 (Fig. 9e) shows that almost the entire surface is coloured in green. A small area at the

lower part area of Las Atalayas (southwest) shows a significant change with respect to its surrounding points (Fig. 9e), which corresponds to an industrial facility built in 2012.

3.1.4 Serra Llarga

The top view of the generated 3DPCs for stages 1, 2 and 3 is shown in Figs. 10a, 10b and 10c, respectively, and the area contains an inactive quarry. The relative height difference of the compared DEMs is shown in Figs. 10d and 10e. An extensive area presented significant negative variation in height and therefore is coloured in blue. This mountain presents a long shape, and the bedding planes are sub-vertical. Visual inspection identified significant rock extraction in the quarry area, which caused a relevant morphological change defined by 50 m height steeped rock slopes; the mountain has almost completely disappeared. Fig. 10e shows that most of the surface is coloured in dark green and the colour is more homogeneous than in the previous comparison. The centre part of the image shows two blue areas (corresponding to negative changes). However, it was verified that those height changes were not due to any extraction activity, but to temporary filling of materials.

The green line in Figs. 10a-c corresponds to the transect shown in Fig. 10f. From 0 to 50 m, distances between stages almost coincided with the stable area. From 50 to 450 m, quarry activity could be observed, where the surface level descended from 30 to 35 m during 1993-2009, but only descended 1 m in 2009-2014. The first descent was caused by the extraction of material, but the second negative change could be due to extractions or errors.

3.1.5 Serra Mitjana

The relative height difference of the compared DEMs is shown in Fig. 11d. Most of the area is coloured in green, yellow and clear blue, which correspond to height difference variations between -5 and 5 m. This reveals a significant DEM error on steep slopes when using old aerial photos. A wide area in the centre of Fig. 11d is coloured in dark blue and violet, presenting height differences from -30 m to -70 m, corresponding to an active quarry. The upper part of Fig. 11d shows an unexpected significant change (in red, positive), and visual inspection confirmed the presence of a landfill, which is located close to a gypsum factory. Height differences between stages 2 and 3 are shown in Fig. 11e. Most of the surface is coloured in dark green, which corresponds to stable areas. The quarry area is represented in dark blue, which corresponds to negative changes, meaning that that rock extraction continued during this period. Finally, the unexpected landfill (upper part of the image) continues increasing in height, presenting yellow points surrounded by dark green points.

3.1.6 Serra de Fontcalent

The relative height difference of the compared DEMs is shown in Figs. 12d and 12e. A wide area of Figs. 12d and 12e can be considered “stable area” and is represented in green; distance ranges from ±5 m are represented in yellow and

light blue, respectively. This demonstrates a significant DEM error on steep slopes when using old aerial photos. In the NE, a blue and purple area (difference heights from -20 to -70 m) is observed, which corresponds to a quarry where rock extraction occurred. On the left side of the quarry, the red area corresponds to a significant height elevation (+25 m), and visual inspection confirmed the presence of a landfill, and more areas can be found surrounding these quarries. Fig. 12e shows that most height differences vary between ±2 m (dark green colour). Additionally, blue and red areas are identified in the quarry, showing that extraction activities are still carried out.

3.1.7 Estimation of volumes

Four selected areas, which were expected to have not suffered changes, were selected for the estimation of volumes through the generated DEMs. The first area was on the southeast side of Sierra de Fontcalent, with a 2x2 km area. The second area was on the northeast side of Sierra Mitjana, with a 1 km length. The third and fourth areas corresponded to the industrial estate Pla de la Vallonga and were defined by two industrial lots (with industrial buildings that exist since the first stage). The order of magnitude of the extension of these areas was 10 m. Table 2 shows the measured volumes for each stage and area. It is observed that when the order of magnitude was high, the maximum error was under 5% for the first stage, and under 1% for the third stage. However, when the order of magnitude was 10 m, the error increased up to 20% for both stages.

With this information, the volume of rock extracted at the quarry of Serra Mitjana was estimated, using the aforementioned procedure. Firstly, the area corresponding to stage 2, which was located next to the quarry, was used to calculate the volume over a horizontal reference plane, yielding 141 hm^3. This value indicated the order of magnitude, and the expected error was obtained from Table 2 (4.3%). The volume difference between stages 1 and 2 was -11.7 hm^3, and the expected error could be as high as 0.6 hm^3 (5% of 11.7 hm^3). The volume calculation between stages 2 and 3 was -3.6 hm^3, and the expected error could be 0.036 hm^3 (1% of 3.6 hm^3).

3.1.8 Analysis of stable areas

Distance analysis for each area of interest was presented previously, revealing that distances computed in areas where no change was expected could be different from zero and therefore inaccuracies could be embedded in the reconstructed landforms. The stable landform areas corresponding to stages 1 and 3 were compared to the benchmark. This analysis was conducted for four different size areas located at the Serra de Fontcalent, Serra Mitjana and two areas of the real estates. The Serra de Fontcalent extension was 2 km^2 and provided information on the accuracy of widespread areas. The Serra Mitjana extension was 0,8 km^2 and was used to assess another widespread area. The two real estate areas were 13000 m^2 and 18000 m^2, respectively, and were used to assess the accuracy of limited areas.

Fig. 13c shows the normalized histogram for each area and each pair of stages. The probability density function of a normal distribution was calculated and overlaid for each histogram. Respective means (μ) and standard deviation (σ) are shown in the corresponding legend.

4 Discussion

The reconstructed landforms presented several deficiencies that are herein discussed. The reconstructed 3DPC of stage 1 (Fig. 6a) presents some empty areas (in white). A detailed view of the point cloud is shown in Fig. 14c, where the background is coloured in red, and therefore empty areas are seen in red. Figs. 14a and 14b show a zoom of the utilised photos taken on the northeast side of Sierra de Fontcalent, where an empty area in the point cloud is detected (in red). Although both photos correspond to the same area, the colours and the shadow of the mountain vary significantly. The photos were taken at different times, with different sun positions and different shadow distributions. Shadows are represented by a set of black pixels in black and white photos and therefore the areas affected by shadows do not show any contrast. Consequently, the lack of contrast in these areas does not provide information and the SfM-MVS method cannot be successfully applied. This effect is pronounced close to steep surfaces, such as quarries (Figs. 14a and 14b) and when there is a high steep surface (Figs. 14d and 14e). This issue can also occur when there is a cloud between the camera and the ground, or when the original photo is damaged (anthropic or natural degradation).

The date and time of a photo capture should also be considered. The photos used for stage 3 presented the capture date (Fig. 5), and it was observed that photos were captured in five organised lines but on different days. The capture process should be performed with caution as shadows or even construction activities can affect the outcome. Location and seasons also affect shadows. In the studied area, the sun is high in summer and low in winter, and consequently, shadows are shorter and longer, respectively. Photos corresponding to stage 3 were captured in late June, and the shadows did not vary significantly in the photos taken in a short time period. However, the photos corresponding to stage 1 were captured in October, when the sun is lower, and the shadows are longer. If photos are captured with a sufficiently long time interval between them, extension and orientation of shadows can be very different, with the appearance of the aforementioned effects.

Resolution of the source of information for the extraction of GCPs and of the used aerial photos restrain the accuracy of the inserted GCPs, affecting the accuracy of the reconstructed landforms. Herein the ALS-derived point cloud provided by the PNOA project was utilized to extract the GCPs, which presented an estimated spatial resolution of approximately 0.4 pts m^{-2}, so the mean distance between points is approximately 1.5 m. This resolution is lower than what was used by Barrand et at. (2009) (1.15 pts m^{-2}). Despite this limitation in terms of resolution, the PNOA point cloud should not be deemed unworthy for the extraction of GCPs. If the resolution of non-digital black and white aerial photos is considered,

it seems reasonable to extract GCPs from this source of information, as both present close resolutions. Using ALS-derived point clouds to extract GCPs presents an advantage with respect to GPS land survey, as it is possible to extract required GCPs during the process, in a single step, without returning to the field.

The acquisition of GCPs can be a major source of uncertainty, as quantity and location are not previously established, but defined by the user. Considering that the coordinates of a GCP are provided, the accurate introduction of any GCP within the corresponding pixel of a photo requires visual detection of the corresponding feature in the image. Unfortunately, this action cannot be performed if the ground has suffered changes, and therefore there is a temporal discrepancy. Common examples of this issue occur in active quarries, activities in landfills or excavations, constructions, land development processes and even in simple vegetation growth. However, although a feature used as GCP is detected, its coordinates could have changed between stages. An important example of this type of changes are landslides, in which X, Y and Z coordinates could have significantly changed. Another example are subsiding areas, where despite the fact that the X and Y coordinates of a control point might not have changed, elevation Z could have suffered variations of up to some tens of cm per year. The introduction of wrong coordinates will lead to errors in the results.

If the pixel size of stage 1 is considered, a precise and accurate extraction of points would not improve the process, as GCPs cannot be inserted accurately. Additionally, the images of this stage are in grayscale, and therefore features are more difficult to detect than when using real colour images. Visual detection and location of a point are hindered, and significant errors are introduced. However, stage 3 offers higher resolution images with true colour pixels, approximately 0.22 m in size, enabling the more accurate introduction of GCPs. The use of recent digital images yields a more accurate reconstruction of the surface when using this methodology.

Fig. 15 shows an example of this procedure, where the extraction of GCPs from the ALS-derived cloud results in a rough selection. Difficulties arise when attempting to match features with its corresponding pixels because of the low resolution of non-digital scanned photos. This low precision occurs because: (1) the used benchmark has a point spacing between 1 and 2 m (Fig. 15), and (2) in stage 1 the pixel size of digitised photos is close to 1 m. The accuracy of the marked points presents a limitation, and therefore the generated model also presents an embedded error. In Fig. 15, the estimated error of GCP number 121 was 7.25 m and 0.32 px, while the estimated error for the GCP number 72 was 4.65 m and 1.57 px.

In addition to the accuracy of the GCPs coordinates, the resolution of the utilised photos plays a key role in the accuracy of GCP introduction. With respect to stage 1, the printed photos were scanned (improved results could have been obtained if the negatives had been scanned with better equipment). Upon payment, some public agencies provide historical aerial photos as scanned images of the negative. However, the goal of this study was to use only common and freely available resources, and therefore this paid option was not considered.

Another important issue that arises during the utilisation of aerial images is the error derived from the existence of monotonous and repetitive areas. Several examples can be found in the results herein presented, such as railway ballast surface or extensive crops. In those areas, the method experienced difficulties to recognize common points between photos, and the generated point cloud presented significant errors in terms of elevations. This issue was found for stages 1 and 3. Fig. 16 presents an example of this issue: at stage 1 the points show the original elevation of the terrain, at stage 2 the railway was under construction, and at stage 3 the railway construction had finished. Fig. 16 shows that in some areas, the elevation of the surface is unreal, approximately 7 meters over the theoretical level. Several attempts were made to correct this situation by inserting tie points. Although this improved the results slightly, it was not possible to eliminate the error. A possible solution is to break the monotonous pattern by inserting external agents (e.g., artificial targets). However, as the intention is to utilise historical images, this solution cannot be applied.

The generated DEMs reproduce the surface of a past stage, providing the possibility of improved visual inspection in comparison with the use of the stereoscopes. In addition to the 3D georeferenced information, the colour of the pixels is also inserted into the model. The use of a digital model enables the possibility of generating contour lines, transects and carrying out even more advanced analysis such as the delimitation of geomorphologic features (e.g. river basins, landslides, etc.).

The analysis of the stable areas showed that the DEMs generated using old aerial black and white photos are more inaccurate than those generated using recently acquired, high-resolution digital aerial photos. The order of magnitude of the analysed area is also relevant to DEM accuracy. Once stages 1 and 3 were generated, both were compared to the benchmark (stage 2). Concerning stage 1, when a large scale is considered, statistical parameters of errors are μ=5 m and σ=3.5 m. When a small scale is considered, statistical parameters are μ =1.5 m and σ=2.5 m. When stage 3 is considered, the errors were significantly lower: when a large scale is considered, μ=0.5 m and σ=1.5 m, and when a low scale is considered, μ=1.5 m and σ=1.5 m (Fig. 13). The use of the generated DEMs to measure geomorphological features definitely depends on the required precision and the scope of the work. For instance, the presented errors could be acceptable to estimate the evolution of areas throughout decades in large glaciers, but this could not be applicable to small active landslides, where the error could have the same order of magnitude of the extension and displacements.

A priori, the errors shown in Fig. 13 suggest that the measured changes are unreliable. Nevertheless, the error can also be analysed by comparing the mapping of the surface with respect to a reference surface, using an adequate colour scale. This representation shows a relatively constant error in terms of sign and magnitude for wide areas (Figs. 7 to 12d and 12e). Moreover, the observation of this colour map shows that, in specific areas, a significant colour change is observed at inactive quarries (Figs. 10 to 12d and 12e), waste treatment plants (Figs. 8d and 8e), constructions (Figs. 7d and 7e) and even new buildings (Figs. 9d and 9e). On one hand, these results suggest that large volumes can be estimated at past

stages and special attention must be paid to the uncertainty inserted by the DEMs errors. On the other hand, despite these errors, the comparison of DEMs showed that changes could be detected. Activities in quarries, soil works (excavations and fillings) and construction of infrastructures and buildings were clearly detected.

5 Conclusions

The use of aerial photos from two different sources of information resulted in the reconstruction of two DEMs for two stages, using data collected and downloaded from public and free access repositories, employing a commercial SfM-MVS software. DEMs enabled the visual inspection of the landform at different stages, and comparison enabled the monitoring of the long-term evolution.

Drawbacks associated with the scanning process of printed historical images were identified: (1) difficulties when attempting to insert GCPs because of photo resolution or the benchmark used to extract the GCPs; (2) impossibility of reconstructing specific areas because of shadows and its variations depending on the date and time; (3) inherent difficulties of the method to reconstruct monotonous areas; (4) height difference of the reconstructed landform with respect to the benchmark (means of 5 and 2 m for large and small scales, respectively); and (5) volume quantification (variations of 4% and 20%, for large and small scales, respectively). Black and white printed aerial photos were used, as well as recently acquired digital aerial photos. When using the latter, better results were obtained: (1) precise RGB colours; (2) higher point cloud resolution; (3) lower height difference with respect to the benchmark (mean of 0.5 m and 1.5 m for large and small scales, respectively); and (4) volume quantification (variations of 1% and 15% for large and small scales, respectively).

The available historic datasets used to reconstruct the DEMs contribute to the study of past processes; locations that count with aerial photo archives can investigate landform evolution or dynamics throughout time. The methodology presented herein is an upgrade to the use of traditional stereoscopes.

The present study makes several noteworthy contributions to the utilisation of historical images for the detection of natural or anthropogenic surface changes. There are limitations, however, regarding the scale of the changes, required precision and characteristics of available data (quality of the aerial images and precision of the GCPs). Herein it was demonstrated that: (1) larger scales yielded lower relative errors of the DEM with respect to the benchmark and (2) better quality of the photos yielded lower relative errors. Consequently, the DEMs generated with this methodology and using old and recent aerial images can be applied to analyse the long-term geomorphology evolution of extensive formations (e.g., mountains, glaciers, and river basins). Not only qualitative analyses can be performed at each stage with 3D-coloured DEM, but existing quantitative methods can be applied to analyse DEMs and detect contour lines, drainage basins or calculate slopes.

The comparison of each DEM with respect to a benchmark enabled the detection of changes due to quarry activities and the estimation of the extracted volumes, new constructions, fillings in solid waste treatment plants, and even the excavation of new cells and construction of new industrial buildings. This demonstrated that the evolution of medium-sized areas (10x10 m landslide, for example) could be monitored, enabling the detection of vertical significant changes but not its accurate quantification. Another contribution of the study herein presented is that local agencies will benefit from this methodology as it enables the identification, location, and quantification of landfills, regardless of their legal status.

The methodology proposed herein is a new element to be added to the toolbox of geomorphologists, and the findings presented further extend the scientific literature on the potential utilisation of readily-available resources.

6 Acknowledgements

This work was partially funded by the University of Alicante (vigrob-157 Project, GRE14-04 and GRE15-19 Project), the University of Florence, the Spanish Ministry of Economy and Competitiveness (MINECO) and EU FEDER, under Projects TIN2014-55413-C2-2-P and TIN2014-55413-C2-2-P. The authors would like to thank the Geography Institute of the University of Alicante, who kindly provided the 1993 aerial images used herein, and Servicios Politécnicos Aéreos SA who provided specifications of the used cameras. Thanks are extended to Mr. José Martínez from Geobit Consulting SA, Pedro Miguel Moya and Dr. Tomás Martínez from the University of Alicante, Dr. Luis Angel Alonso Matilla and Julio Company Rodríguez from the Universitat Politècnica de València and Dr. Antonio Abellán from the University of Cambridge, for their stimulating discussions at the early stages of this manuscript.

7 Appendix A: Processing parameters of SfM-MVS.

8 References

Agisoft LLC (2016a) Agisoft Photoscan User Manual: Professional Edition, V 1.2. Agisoft LLC

Agisoft LLC (2016b) AgiSoft PhotoScan Professional edition. AgiSoft LLC

Barrand NE, Murray T, James TD, Barr SL, Mills JP (2009) Optimizing photogrammetric DEMs for glacier volume change assessment using laser-scanning derived ground-control points. J Glaciol 55:106–116 . doi: 10.3189/002214309788609001

Brasington J, Rumsby BT, McVey RA (2000) Monitoring and modelling morphological change in a braided gravel-bed river using high resolution GPS-based survey. Earth Surf Process Landforms 25:973–990

Brodu N, Lague D (2012) 3D point cloud classification of complex natural scenes using a multi-scale dimensionality criterion: applications in geomorphology. In: EGU General Assembly Conference Abstracts. p 4368

Brückl E, Brunner FK, Kraus K (2006) Kinematics of a deep‐seated landslide derived from photogrammetric, GPS and geophysical data. Eng Geol 88:149–159 . doi: 10.1016/j.enggeo.2006.09.004

Cano M (2003) Consideraciones acerca de la sierra de Fontcalent y sus canteras. Actuaciones puntuales en su restauración. Trabajo Fin de Carrera de Ingenería Geológica.

Chandler JH, Brunsden D (1995) Steady state behaviour of the black ven mudslide: The application of archival analytical photogrammetry to studies of landform change. Earth Surf Process Landforms 20:255–275 . doi: 10.1002/esp.3290200307

Chandler JH, Moore R (1989) Analytical photogrammetry: a method for monitoring slope instability. Q J Eng Geol Hydrogeol 22:97–110 . doi: 10.1144/GSL.QJEG.1989.022.02.02

Cook KL (2017) An evaluation of the effectiveness of low-cost UAVs and structure from motion for geomorphic change detection. Geomorphology 278:195–208 . doi: 10.1016/j.geomorph.2016.11.009

Eltner A, Kaiser A, Castillo C, Rock G, Neugirg F, Abellán A (2016) Image-based surface reconstruction in geomorphometry – merits, limits and developments. Earth Surf Dyn 4:359–389 . doi: 10.5194/esurf-4-359-2016

Engel J, Koltun V, Cremers D (2017) Direct Sparse Odometry. IEEE Trans Pattern Anal Mach Intell 1–1 . doi: 10.1109/TPAMI.2017.2658577

Engel J, Schöps T, Cremers D (2014) LSD-SLAM: Large-scale direct monocular SLAM. In: European Conference on Computer Vision. pp 834–849

Fisher RB, Breckon TP, Dawson-Howe K, Fitzgibbon A, Robertson C, Trucco E, Williams CKI (2013) Dictionary of computer vision and image processing. John Wiley & Sons

Generalitat Valenciana (1993a) IDE de la Comunitat Valenciana - ICV. http://catalogo.icv.gva.es/geonetwork/srv/spa/catalog.search#/metadata/spaicvvuelo93As2015. Accessed 29 Dec 2016

Generalitat Valenciana (1993b) [Fotografía aérea de la provincia de Alicante: vuelo 1993] TT -. TA - 20 carpetas.

Generalitat Valenciana (2016) Fototeca ICV. In: Terrasit, ICV. http://fototeca.icv.gva.es/?vuelo=VF_1993_Sur_Alicante_25000_pan. Accessed 29 Dec 2016

Girardeau-Montaut D (2016) CloudCompare (version 2.8) [GPL software]. OpenSource Proj.

Gomez C (2014) Digital photogrammetry and GIS-based analysis of the bio-geomorphological evolution of Sakurajima Volcano, diachronic analysis from 1947 to 2006. J Volcanol Geotherm Res 280:1–13 . doi:

10.1016/j.jvolgeores.2014.04.015

Gomez C, Hayakawa Y, Obanawa H (2015) A study of Japanese landscapes using structure from motion derived DSMs and DEMs based on historical aerial photographs: New opportunities for vegetation monitoring and diachronic geomorphology. Geomorphology 242:11–20 . doi: 10.1016/j.geomorph.2015.02.021

Hapke CJ (2005) Estimation of regional material yield from coastal landslides based on historical digital terrain modelling. Earth Surf Process Landforms 30:679–697 . doi: 10.1002/esp.1168

Hartley R, Zisserman A (2003) Multiple view geometry in computer vision. Cambridge university press

Hsieh Y-C, Chan Y-C, Hu J-C (2016) Digital Elevation Model Differencing and Error Estimation from Multiple Sources: A Case Study from the Meiyuan Shan Landslide in Taiwan. Remote Sens 8:199 . doi: 10.3390/rs8030199

INGEMISA, Aurenheimer C (1991) Mapa geocientífico de la provincia de Alicante

Instituto Geográfico Nacional (2016) Centro de Descargas del CNIG (IGN). http://centrodedescargas.cnig.es/CentroDescargas/catalogo.do#selectedSerie. Accessed 28 Dec 2016

Instituto Geográfico Nacional de España (2016) Plan Nacional de Ortofotografía Aérea (PNOA). http://pnoa.ign.es/presentacion. Accessed 9 Sep 2016

Ishiguro S, Yamano H, Oguma H (2016) Evaluation of DSMs generated from multi-temporal aerial photographs using emerging structure from motion–multi-view stereo technology. Geomorphology 268:64–71 . doi: 10.1016/j.geomorph.2016.05.029

James MR, Robson S (2012) Straightforward reconstruction of 3D surfaces and topography with a camera: Accuracy and geoscience application. J Geophys Res Earth Surf 117:n/a-n/a . doi: 10.1029/2011JF002289

James MR, Robson S (2014) Mitigating systematic error in topographic models derived from UAV and ground-based image networks. Earth Surf Process Landforms 39:1413–1420 . doi: 10.1002/esp.3609

Kjeldsen KK, Korsgaard NJ, Bjørk AA, Khan SA, Box JE, Funder S, Larsen NK, Bamber JL, Colgan W, van den Broeke M, Siggaard-Andersen M-L, Nuth C, Schomacker A, Andresen CS, Willerslev E, Kjær KH (2015) Spatial and temporal distribution of mass loss from the Greenland Ice Sheet since AD 1900. Nature 528:396–400 . doi: 10.1038/nature16183

Krizhevsky A, Sutskever I, Hinton GE (2012) ImageNet Classification with Deep Convolutional Neural Networks. In: Pereira F, Burges CJC, Bottou L, Weinberger KQ (eds) Advances in Neural Information Processing Systems 25. Curran Associates, Inc., pp 1097–1105

Lague D, Brodu N, Leroux JJ (2013) Accurate 3D comparison of complex topography with terrestrial laser scanner: Application to the Rangitikei canyon (NZ). ISPRS J Photogramm Remote Sens 82:10–26 . doi: 10.1016/j.isprsjprs.2013.04.009

Midgley NG, Tonkin TN (2017) Reconstruction of former glacier surface topography from archive oblique aerial images. Geomorphology 282:18–26 . doi: 10.1016/j.geomorph.2017.01.008

Niethammer U, James MRMR, Rothmund S, Travelletti J, Joswig M (2012) UAV-based remote sensing of the Super-Sauze landslide: Evaluation and results. Eng Geol 128:2–11 . doi: 10.1016/j.enggeo.2011.03.012

Purdie H, Bealing P, Tidey E, Gomez C, Harrison J (2016) Bathymetric evolution of Tasman Glacier terminal lake, New Zealand, as determined by remote surveying techniques. Glob Planet Change 147:1–11 . doi: 10.1016/j.gloplacha.2016.10.010

Razak KA, Straatsma MW, van Westen CJ, Malet J-P, de Jong SM (2011) Airborne laser scanning of forested landslides characterization: Terrain model quality and visualization. Geomorphology 126:186–200 . doi: 10.1016/j.geomorph.2010.11.003

Rusu RB, Marton ZC, Blodow N, Dolha M, Beetz M (2008) Towards 3D Point cloud based object maps for household environments. Rob Auton Syst 56:927–941 . doi: 10.1016/j.robot.2008.08.005

Snavely N, Seitz SM, Szeliski R (2008) Modeling the World from Internet Photo Collections. Int J Comput Vis 80:189–210 . doi: 10.1007/s11263-007-0107-3

Su W-J, Stohr C (2000) Aerial-photointerpretation of landslides along the Ohio and Mississippi rivers. Environ Eng Geosci 6:

Szeliski R (2010) Computer vision: algorithms and applications. Springer Science & Business Media

Tonkin T, Midgley N (2016) Ground-Control Networks for Image Based Surface Reconstruction: An Investigation of Optimum Survey Designs Using UAV Derived Imagery and Structure-from-Motion Photogrammetry. Remote Sens 8:786 . doi: 10.3390/rs8090786

Tonkin TN, Midgley NG, Cook SJ, Graham DJ (2016) Ice-cored moraine degradation mapped and quantified using an unmanned aerial vehicle: A case study from a polythermal glacier in Svalbard. Geomorphology 258:1–10 . doi: 10.1016/j.geomorph.2015.12.019

Tonkin TN, Midgley NG, Graham DJ, Labadz JC (2014) The potential of small unmanned aircraft systems and structure-from-motion for topographic surveys: A test of emerging integrated approaches at Cwm Idwal, North Wales. Geomorphology 226:35–43 . doi: 10.1016/j.geomorph.2014.07.021

U.S. Geological Survey (2000) Report of calibration of Aerial Mapping Camera, Wild RC10

Ullman S (1979) The interpretation of visual motion. Massachusetts Inst of Technology Pr

Vexcel Imaging (2014) Field Calibration Report, UltraCamX, SN UCX-SX-1-50013345. Graz, Austria, Austria

Westoby MJJ, Brasington J, Glasser NFF, Hambrey MJJ, Reynolds JMM (2012) Structure-from-Motion photogrammetry: A low-cost, effective tool for geoscience applications. Geomorphology 179:300–314 . doi:

http://dx.doi.org/10.1016/j.geomorph.2012.08.021

Wu C (2013) Towards linear-time incremental structure from motion. In: 3DTV-Conference, 2013 International Conference on. pp 127–134

Wu C (2011) VisualSFM: A visual structure from motion system

Wu C, Agarwal S, Curless B, Seitz SM (2011) Multicore bundle adjustment. In: Computer Vision and Pattern Recognition (CVPR), 2011 IEEE Conference on. pp 3057–3064

List of figures

Figure 12. Study area: Sierra de Fontcalent. (a) stage 1 (1993) cloud; (b) stage 2 (2009) cloud; (c) stage 3 (2014) cloud; (d) distances between stages 1 and 2; (e) distances between stages 2 and 3. White areas correspond to areas where 3D information was not available after reconstruction.

Figure 13. Normalized histogram of relative height distances. Stable areas of stages 1-2 and stages 2-3: (a) Sierra de Fontcalent; (b) Sierra Mitjana; (c) industrial estate 1; (d) industrial estate 2.

Figure 14. Issues found in stage 1 (1993). (a) and (b) zoom of photos number 5684 and 5742, NE of the mountain; (c) 3DPC generated for stage 1 (1993), where the background is coloured in red, representing areas without points; (b) and (c) zoom of photos number 5684 and 5685, SW of the mountain.

Figure 15. Extraction of ground control points from the ALS point cloud (stage 2) and introduction into photos of stages 1 and 3.

Figure 16. Reconstruction of the railway close to the waste treatment plant. (a) Comparison of stages 1 and 2 and (b) comparison of stages 2 and 3.

List of tables

Appendix A.

Tables

Table 1. Residual Mean Square Error (RMSE) of GCP.

Stage	Count	X error (m)	Y error (m)	Z error (m)	XY error (m)	Total (m)	Image (pix)
1: 1993	150	2.17752	2.80247	3.19653	3.549	4.7763	0.665
3: 2014	294	1.23805	1.51134	1.88215	1.95369	2.7182	2.127

Table 2. Measurement of volumes (hm^3) and variation with respect to stage 2 (%) for four areas: Fontcalent Mountain, Serra Mitjana and I.E. (Industrial Estate) of Pla de la Vallonga.

	Measured Volume (hm^3)				Variation with respect to the reference			
	Fontcalent	Serra Mitjana	I.E. 1	I.E. 2	Fontcalent	Serra Mitjana	I.E. 1	I.E. 2
1 (1993)	305.74	203.8	0.165	0.199	2.5%	4.3%	-9.3%	-20%
2 (2009)	313.175	212.49	0.182	0.249	-	-	-	-
3 (2014)	309.9	213.52	0.208	0.292	1%	0.3%	14.2%	17%

Appendix A

Table A.1 Processing parameters of Agisoft Photoscan applied to stages 1 and 3.

Stage	**1 (1993)**	**3 (2014)**
General		
Cameras	9	56
Aligned cameras	9	55
Markers	150	360
Coordinate system	ETRS89 (30N)	ETRS89 (30N)
Point Cloud		
Points	18636 of 19141	62148 of 73324
RMS reprojection error	0.342198 (0.742668 pix)	0.716126 (1.76596 pix)
Max reprojection error	1.67728 (4.16358 pix)	2.95046 (12.5087 pix)
Mean keypoint size	2.25677 pix	2.50941 pix
Effective overlap	2.2004600000	3.12726
Alignment parameters		
Accuracy	High	High
Pair preselection	Disabled	Disabled
Keypoint limit	40000	40000
Tie point limit	4000	4000
Constrain features bymask	No	No
Adaptive camera model fitting	Yes	Yes
Matching time	26 seconds	19 minutes 37 seconds
Alignment time	0 seconds	29 seconds
Optimization parameters		
Parameters	f, cx, cy	f
Optimization time	0 seconds	1 seconds
Dense Point Cloud		
Points	18369450	148907817
Reconstruction parameters		
Quality	High	Medium
Depth filtering	Aggressive	Aggressive
Depth maps generation time	3 minutes 51 seconds	59 minutes 46 seconds
Dense cloud generation time	37 seconds	15 minutes 59 seconds
Software		
Version	1.2.6 build 2834	1.2.6 build 2834
Platform	*Windows 64 bit*	*Windows 64 bit*

Highlights

Existing techniques enable the use of historical and recent aerial photos to reconstruct DEMS

An area of interest is reconstructed using historical printed and digital aerial photos through Structure-from-Motion

The used data are readily available resources

An airbone LiDAR derived point cloud was used as a benchmark and for the extraction of ground control points

Three different stages of the landform were analysed and compared

The quality of the reconstruction and the capability of monitoring changes were analysed

(a) Location of the area of interest: Alicante, SE Spain.

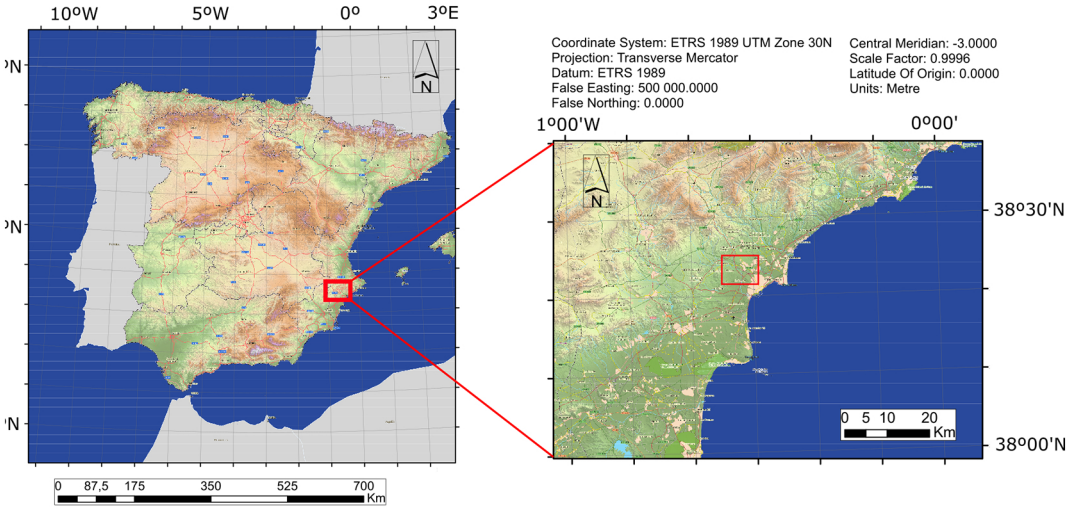

(b) Area of interest: ALS-derived 3DPC

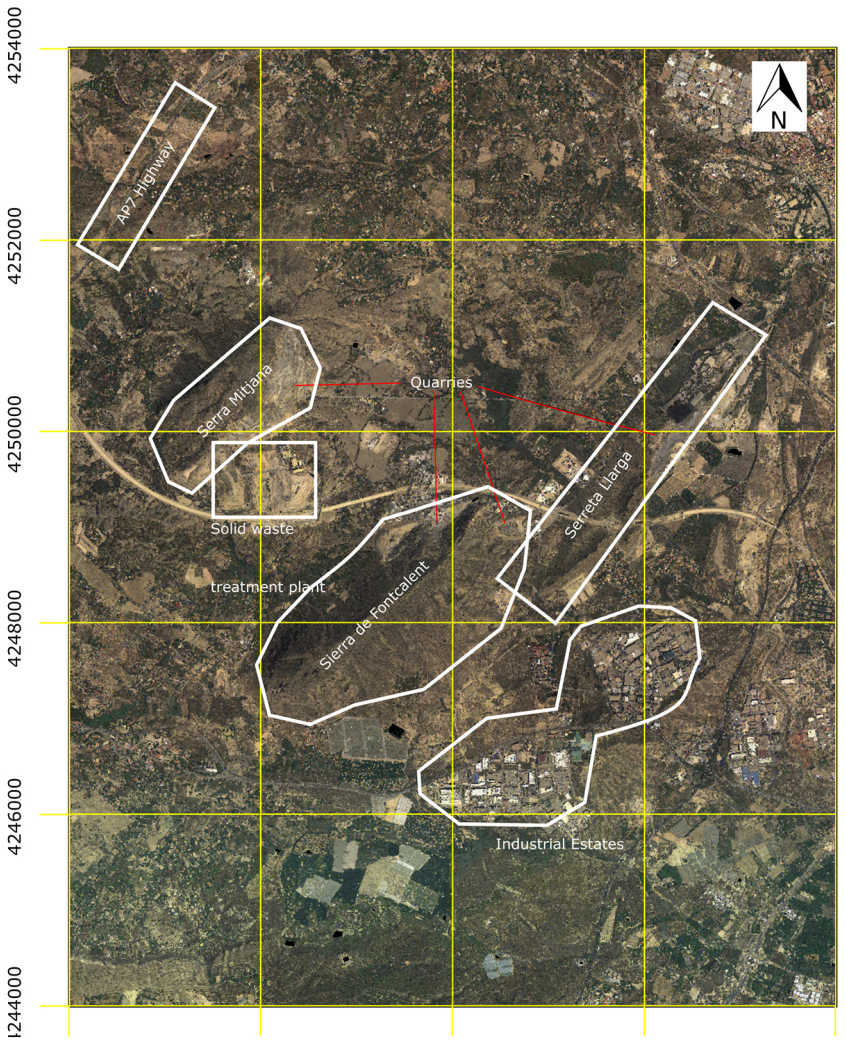

Figure 1

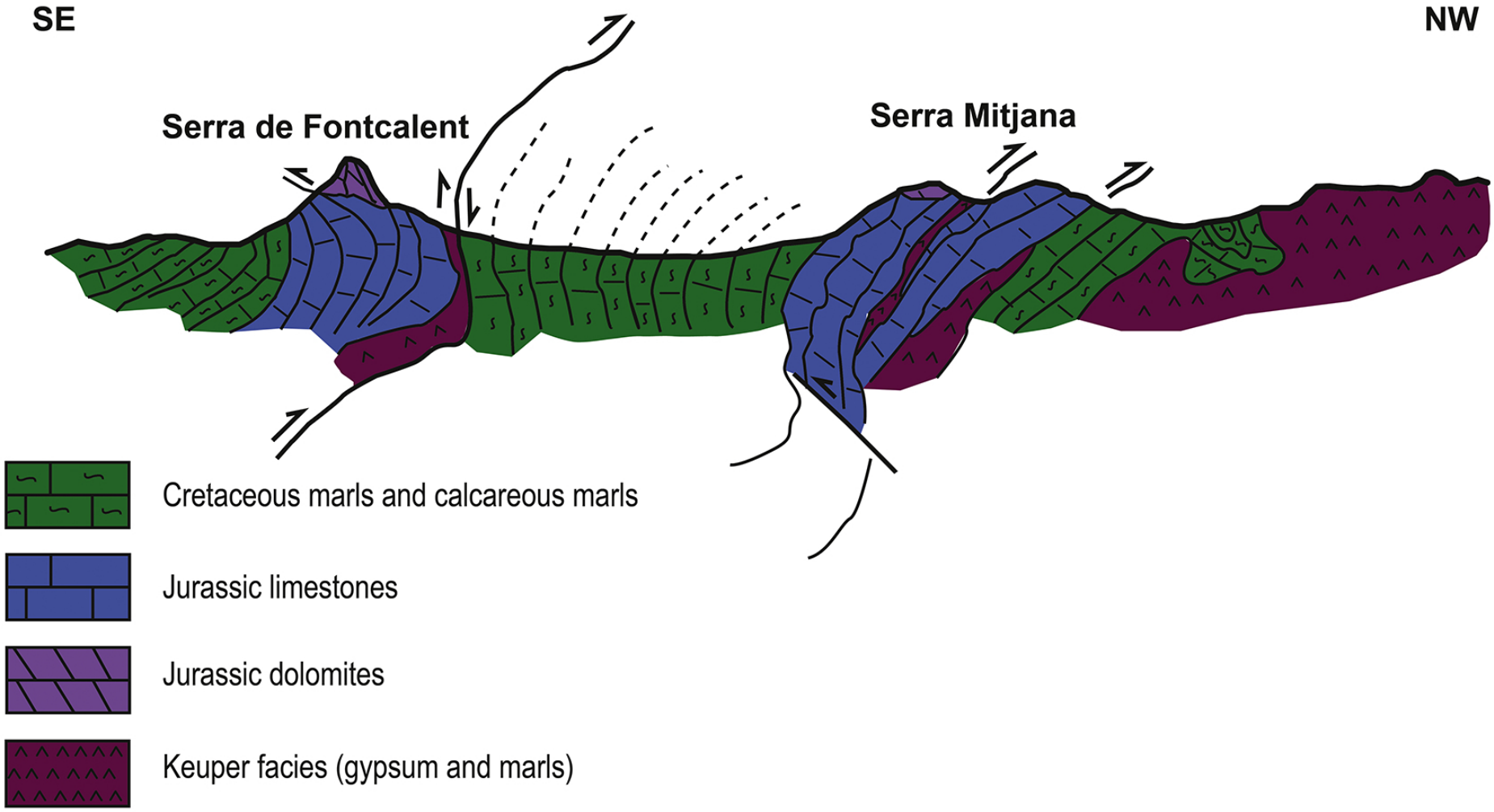
SE
NW
Serra de Fontcalent
Serra Mitjana
Cretaceous marls and calcareous marls
Jurassic limestones
Jurassic dolomites
Keuper facies (gypsum and marls)

Figure 2

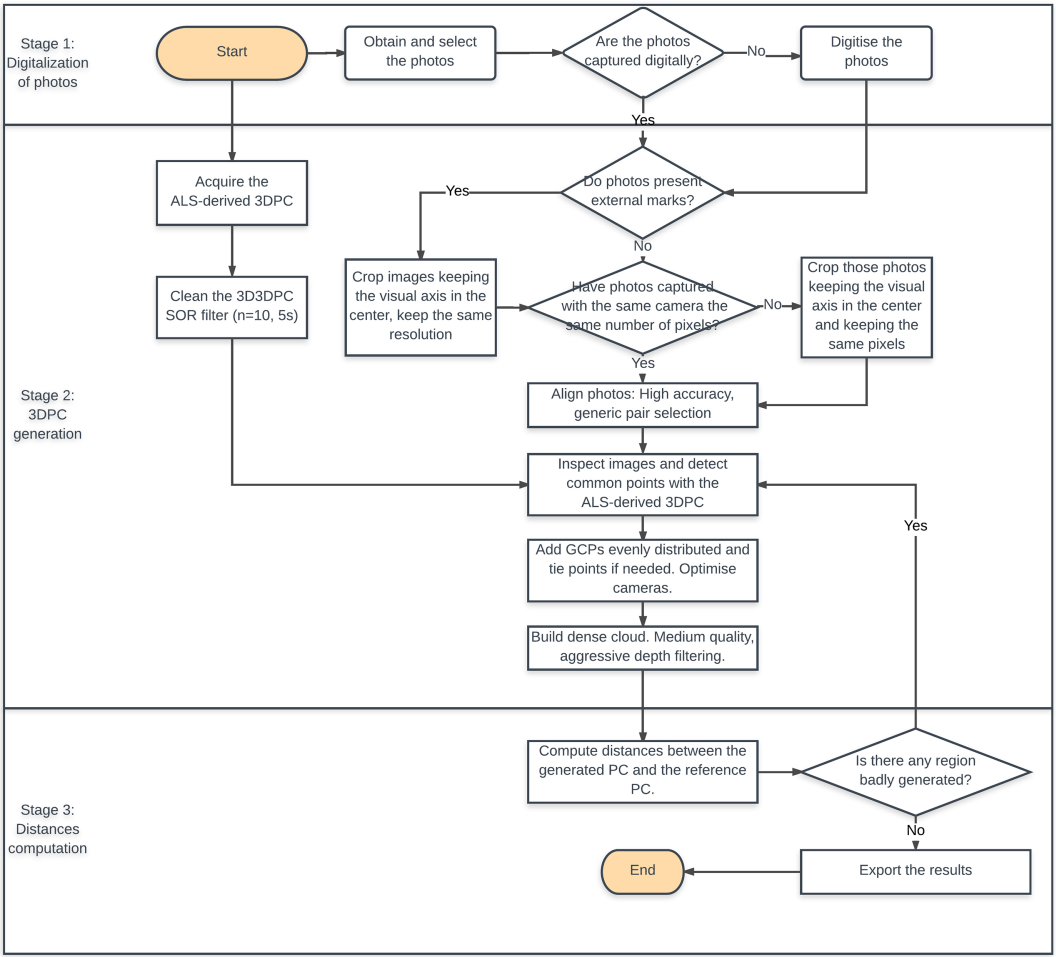
Stage 1: Digitalization of photos
Start
Obtain and select the photos
Are the photos captured digitally?
No
Digitise the photos
Yes
Stage 2: 3DPC generation
Acquire the ALS-derived 3DPC
Do photos present external marks?
Yes
No
Clean the 3D3DPC SOR filter (n=10, 5s)
Crop images keeping the visual axis in the center, keep the same resolution
Have photos captured with the same camera the same number of pixels?
No
Crop those photos keeping the visual axis in the center and keeping the same pixels
Yes
Align photos: High accuracy, generic pair selection
Inspect images and detect common points with the ALS-derived 3DPC
Yes
Add GCPs evenly distributed and tie points if needed. Optimise cameras.
Build dense cloud. Medium quality, aggressive depth filtering.
Stage 3: Distances computation
Compute distances between the generated PC and the reference PC.
Is there any region badly generated?
No
End
Export the results

Figure 3

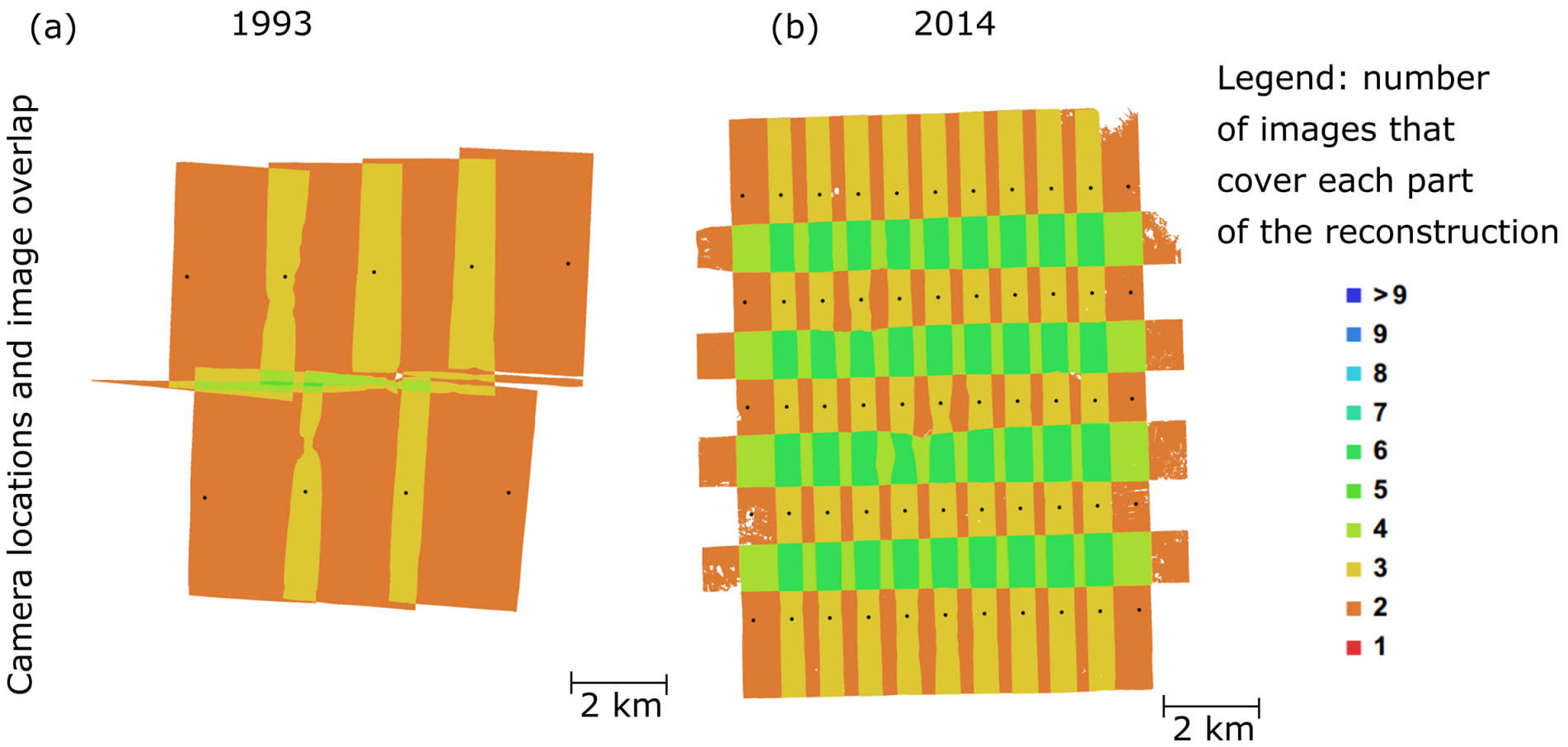
(a)
1993
(b)
2014
Camera locations and image overlap
Legend: number of images that cover each part of the reconstruction
>9
9
8
7
6
5
4
3
2
1
2 km
2 km

Figure 4

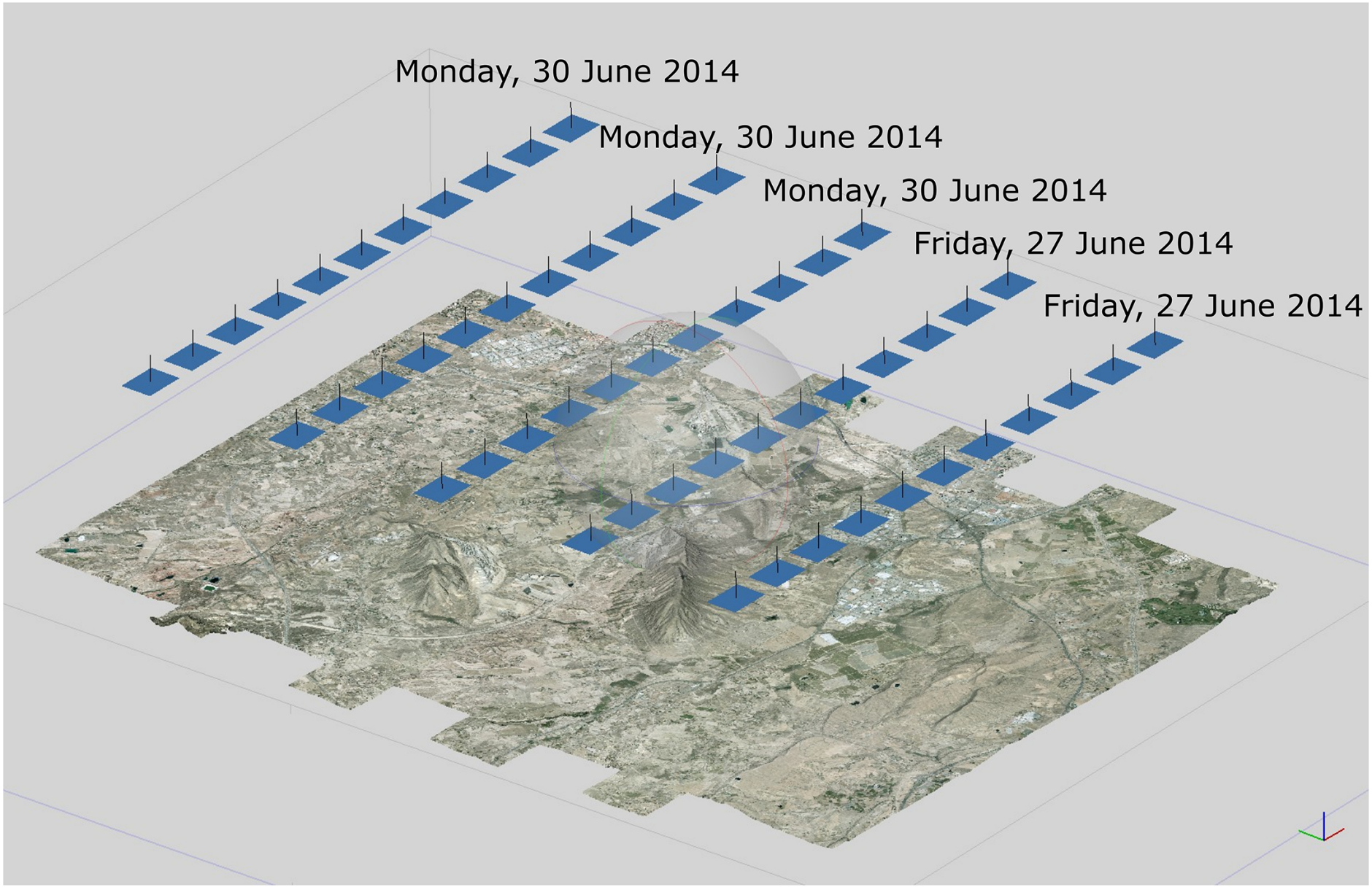
Monday, 30 June 2014
Monday, 30 June 2014
Monday, 30 June 2014
Friday, 27 June 2014
Friday, 27 June 2014

Figure 5

(a) Scenario 1:

non-digital aerial photos, 1993

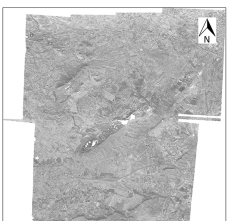

(b) Scenario 2:

ALS-derived 3DPC, 2009

(c) Scenario 3:

digital aerial photos, 2014

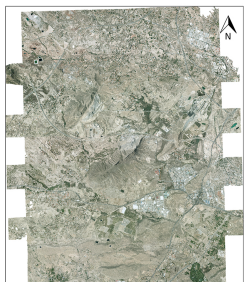

Figure 6

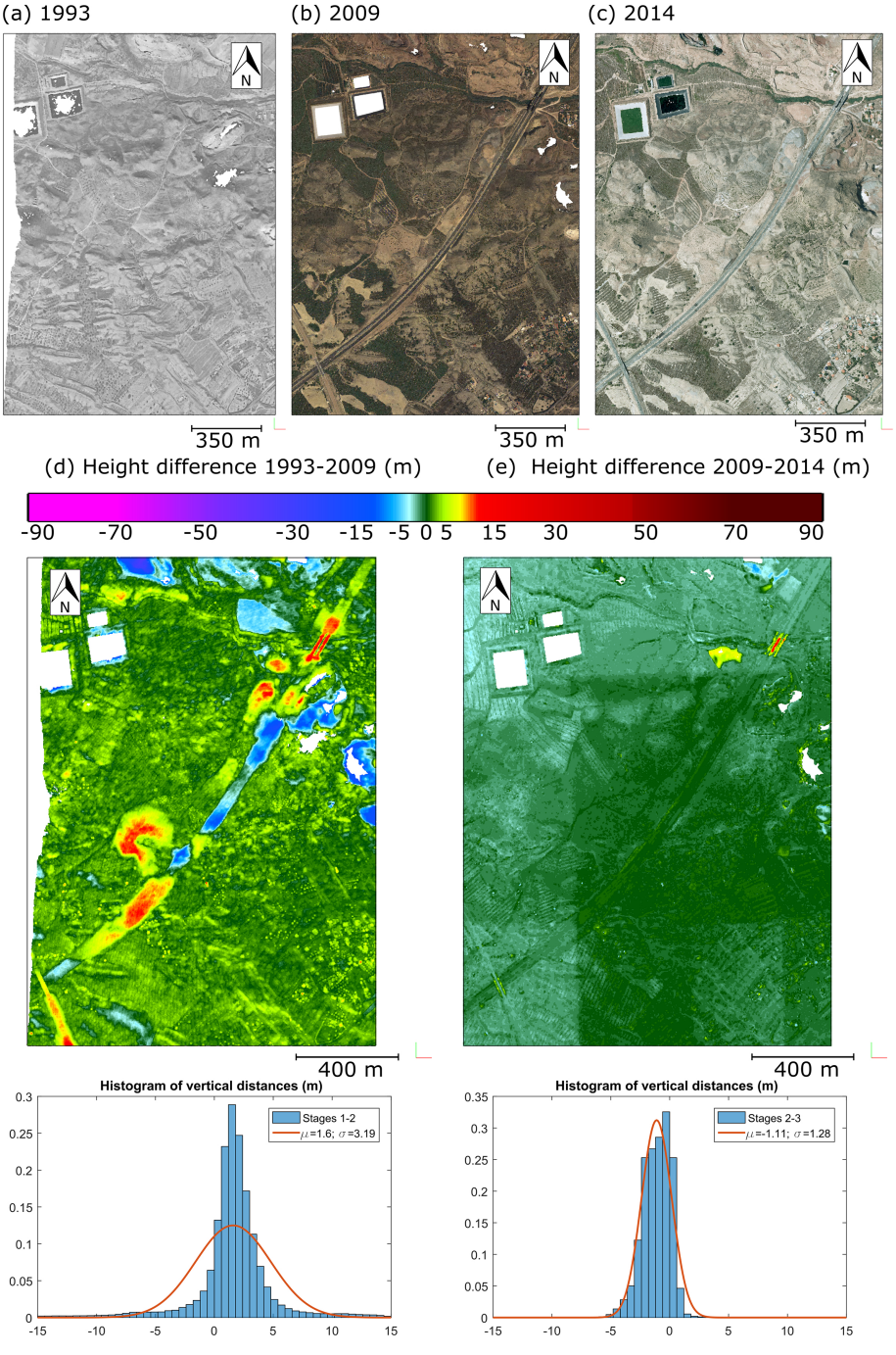
(a) 1993
(b) 2009
(c) 2014
N
350 m
(d) Height difference 1993-2009 (m)
(e) Height difference 2009-2014 (m)
-90 -70 -50 -30 -15 -5 0 5 15 30 50 70 90
400 m
Histogram of vertical distances (m)
Stages 1-2
μ=1.6; σ=3.19
Histogram of vertical distances (m)
Stages 2-3
μ=-1.11; σ=1.28

Figure 7

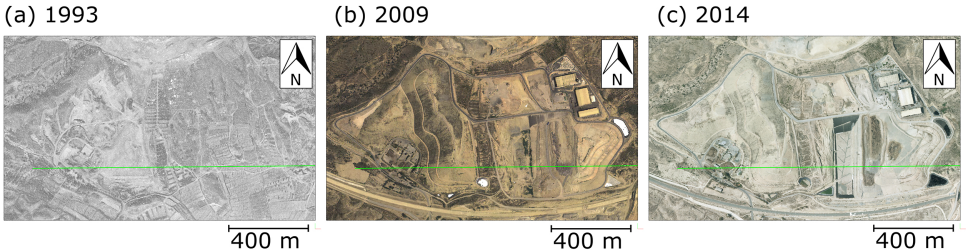
(a) 1993
(b) 2009
(c) 2014
N
400 m

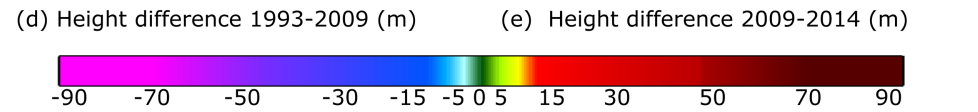
(d) Height difference 1993-2009 (m)
(e) Height difference 2009-2014 (m)
-90 -70 -50 -30 -15 -5 0 5 15 30 50 70 90
N
350 m

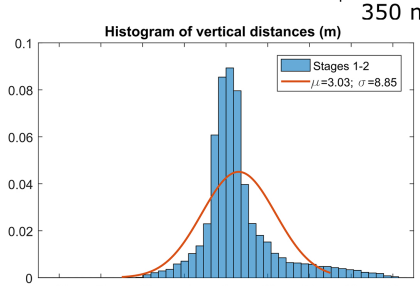
Histogram of vertical distances (m)
Stages 1-2
μ=3.03; σ=8.85

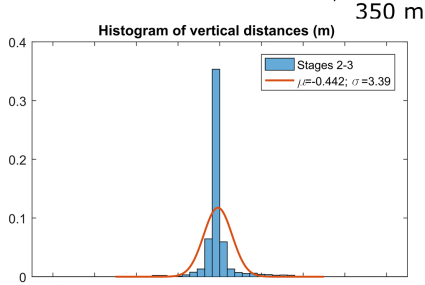
Histogram of vertical distances (m)
Stages 2-3
μ=-0.442; σ=3.39

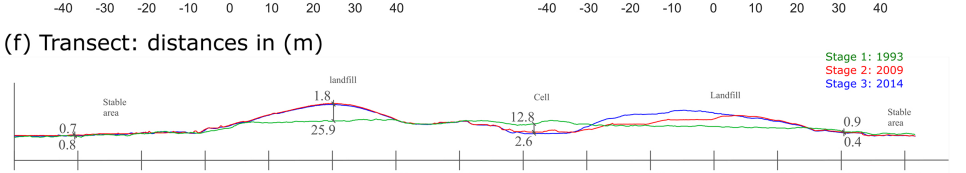
(f) Transect: distances in (m)
Stage 1: 1993
Stage 2: 2009
Stage 3: 2014
Stable area
landfill
Cell
Landfill
Stable area
1.8
25.9
12.8
2.6
0.7
0.8
0.9
0.4

Figure 8

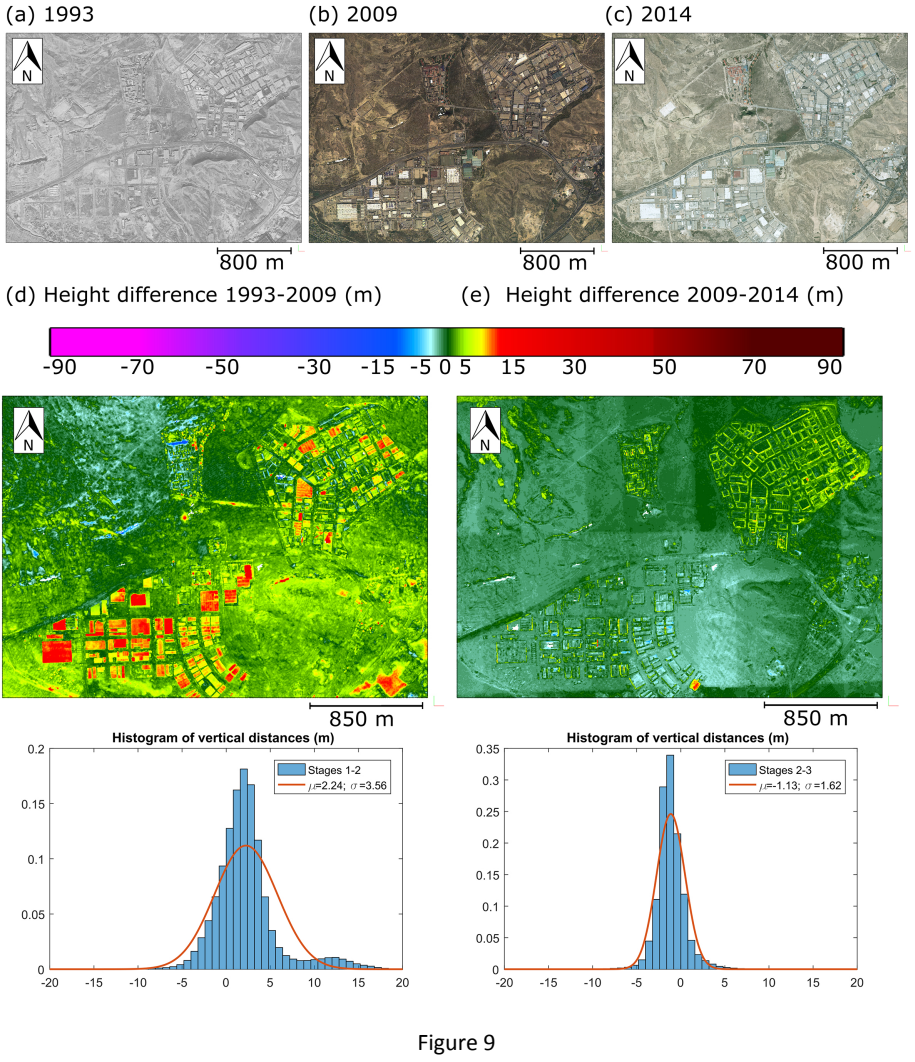
(a) 1993
(b) 2009
(c) 2014
N
800 m
(d) Height difference 1993-2009 (m)
(e) Height difference 2009-2014 (m)
-90 -70 -50 -30 -15 -5 0 5 15 30 50 70 90
850 m
Histogram of vertical distances (m)
Stages 1-2
μ=2.24; σ=3.56
Histogram of vertical distances (m)
Stages 2-3
μ=-1.13; σ=1.62

Figure 9

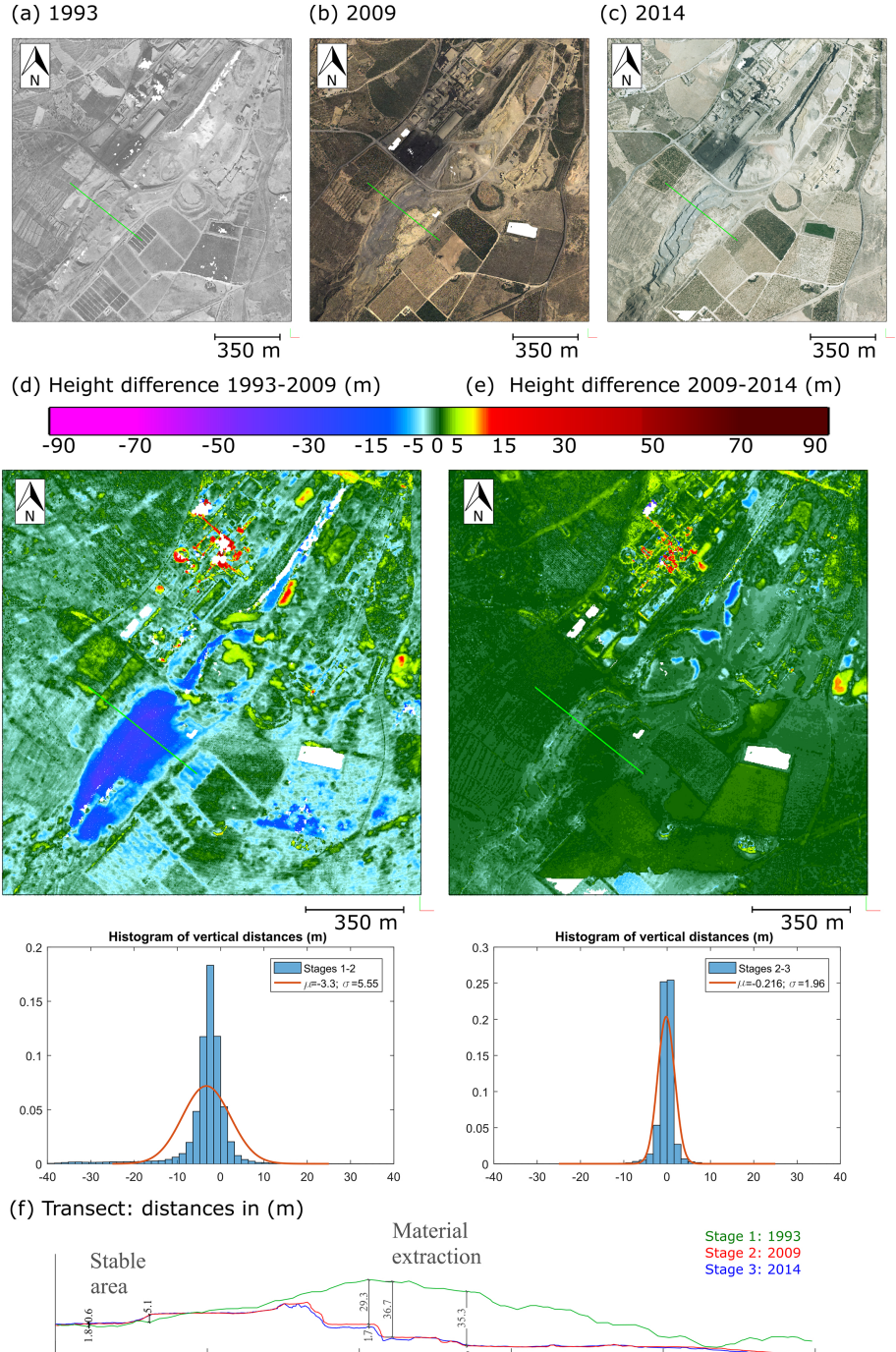
(a) 1993
(b) 2009
(c) 2014
N
350 m
(d) Height difference 1993-2009 (m)
(e) Height difference 2009-2014 (m)
-90 -70 -50 -30 -15 -5 0 5 15 30 50 70 90
Histogram of vertical distances (m)
Stages 1-2
μ=-3.3; σ=5.55
Stages 2-3
μ=-0.216; σ=1.96
(f) Transect: distances in (m)
Stable area
Material extraction
Stage 1: 1993
Stage 2: 2009
Stage 3: 2014
0 100 200 300 400 500

Figure 10

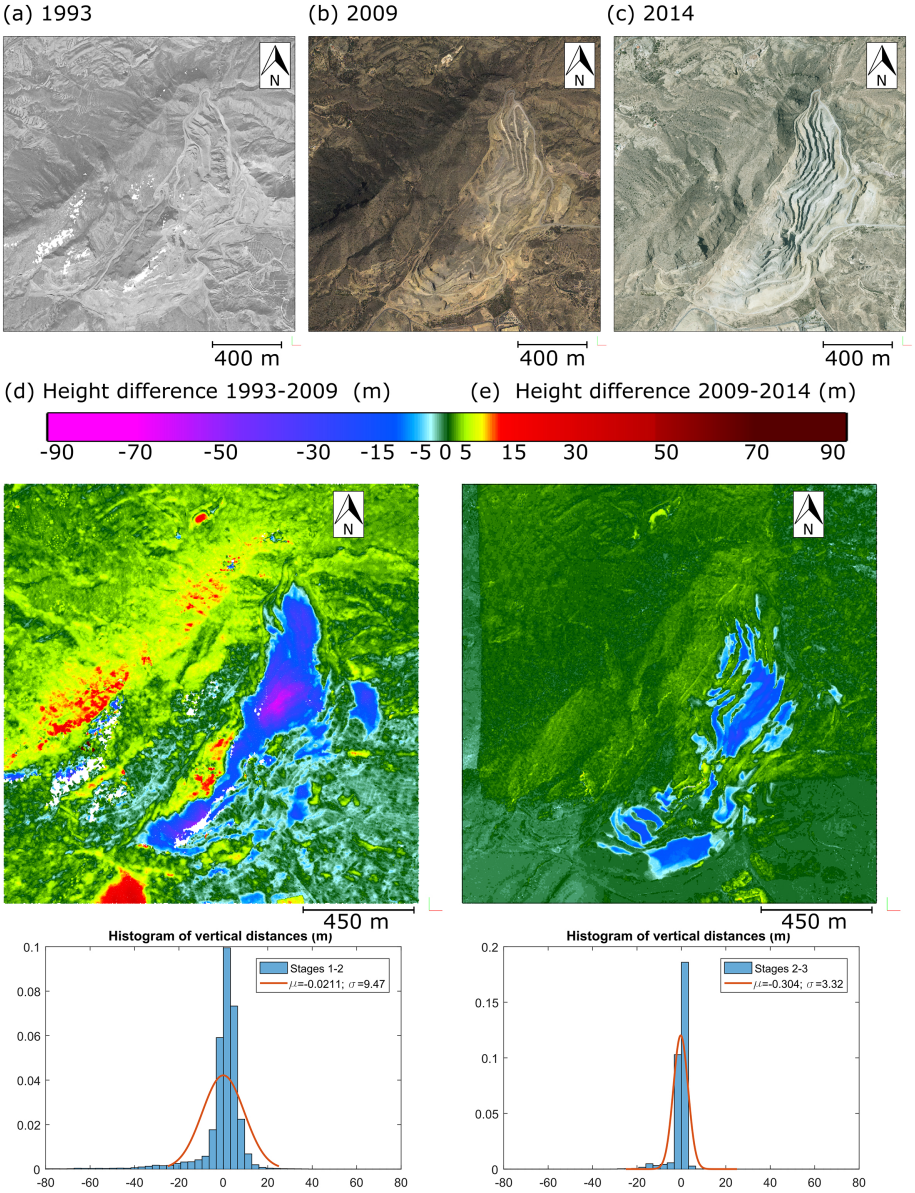
(a) 1993
(b) 2009
(c) 2014
N
400 m
(d) Height difference 1993-2009 (m)
(e) Height difference 2009-2014 (m)
-90 -70 -50 -30 -15 -5 0 5 15 30 50 70 90
450 m
Histogram of vertical distances (m)
Stages 1-2
μ=-0.0211; σ=9.47
Stages 2-3
μ=-0.304; σ=3.32

Figure 11

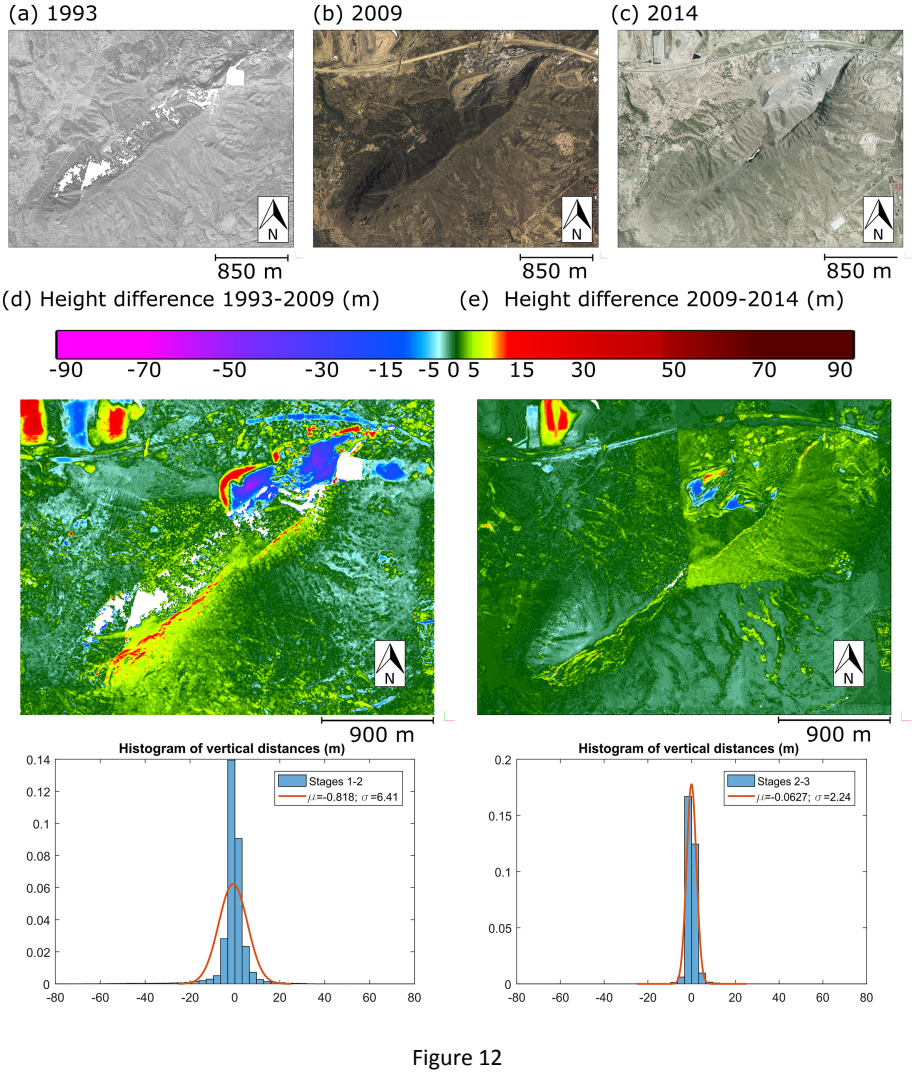
(a) 1993
(b) 2009
(c) 2014
N
850 m
(d) Height difference 1993-2009 (m)
(e) Height difference 2009-2014 (m)
-90 -70 -50 -30 -15 -5 0 5 15 30 50 70 90
900 m
Histogram of vertical distances (m)
Stages 1-2
μ=-0.818; σ=6.41
Stages 2-3
μ=-0.0627; σ=2.24

Figure 12

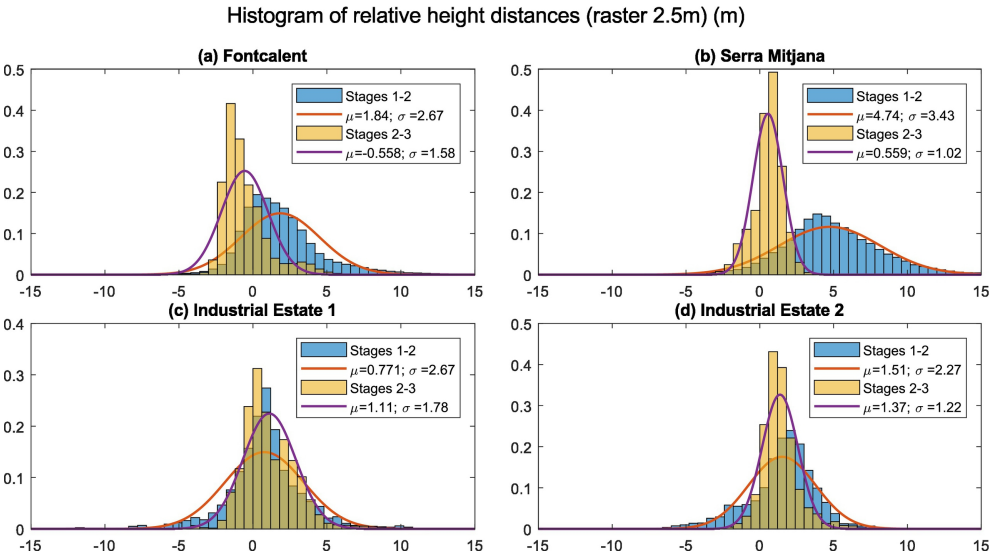
Histogram of relative height distances (raster 2.5m) (m)
(a) Fontcalent
Stages 1-2
μ=1.84; σ =2.67
Stages 2-3
μ=-0.558; σ =1.58
(b) Serra Mitjana
Stages 1-2
μ=4.74; σ =3.43
Stages 2-3
μ=0.559; σ =1.02
(c) Industrial Estate 1
Stages 1-2
μ=0.771; σ =2.67
Stages 2-3
μ=1.11; σ =1.78
(d) Industrial Estate 2
Stages 1-2
μ=1.51; σ =2.27
Stages 2-3
μ=1.37; σ =1.22

Figure 13

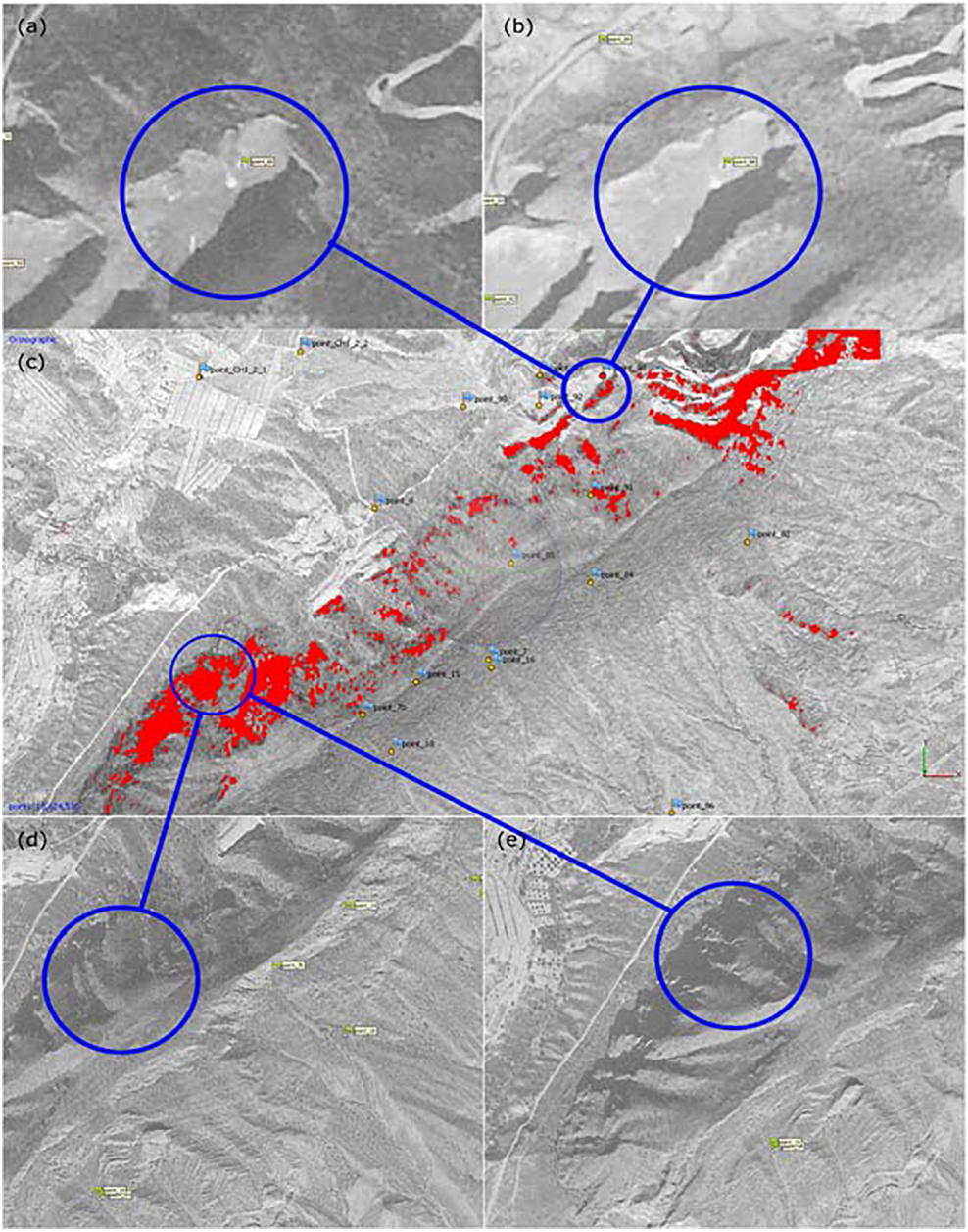

Figure 14

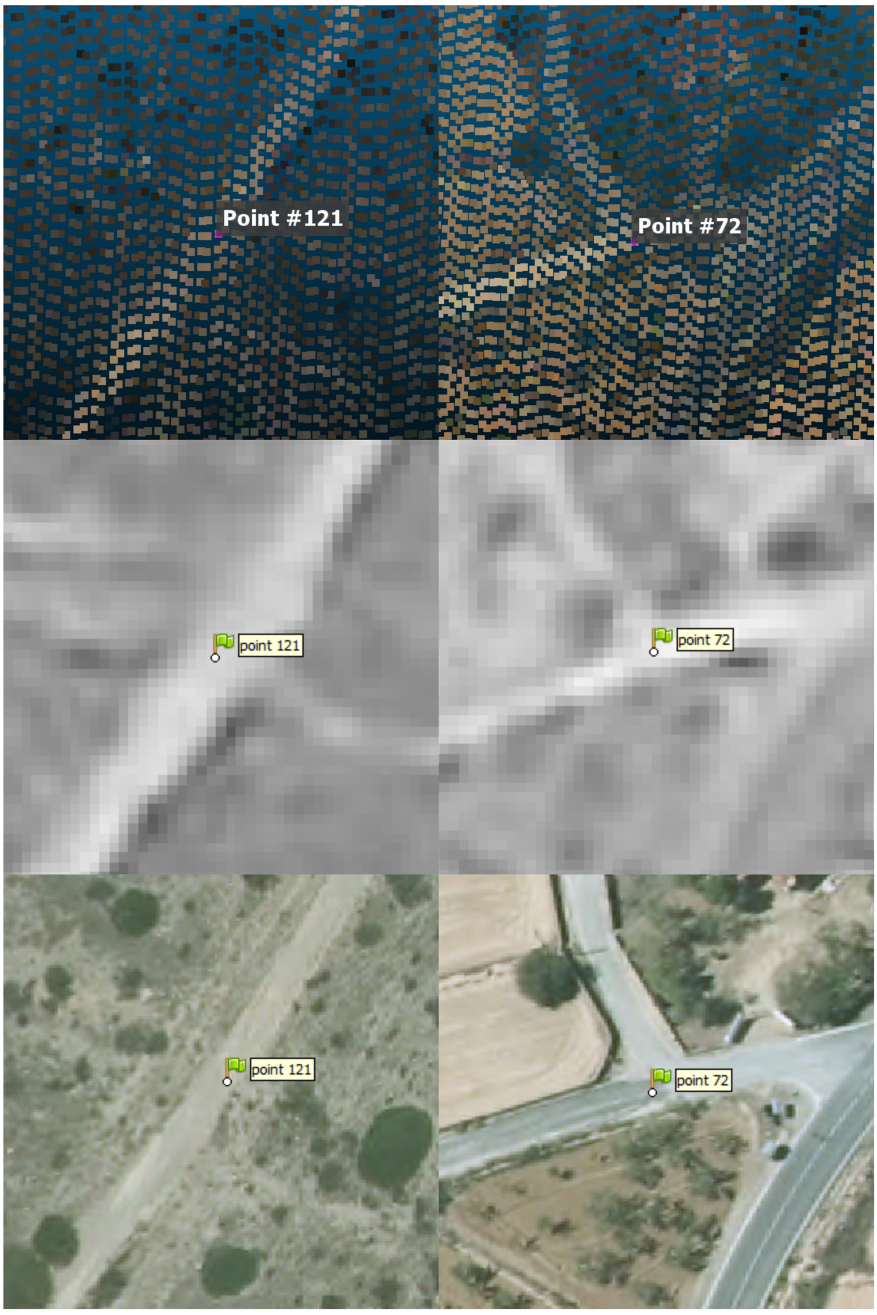
Point 121
Point 72
Stage 2: 2009
Stage 1: 1993
Stage 3: 2014
Point #121
Point #72
point 121
point 72
point 121
point 72

Figure 15

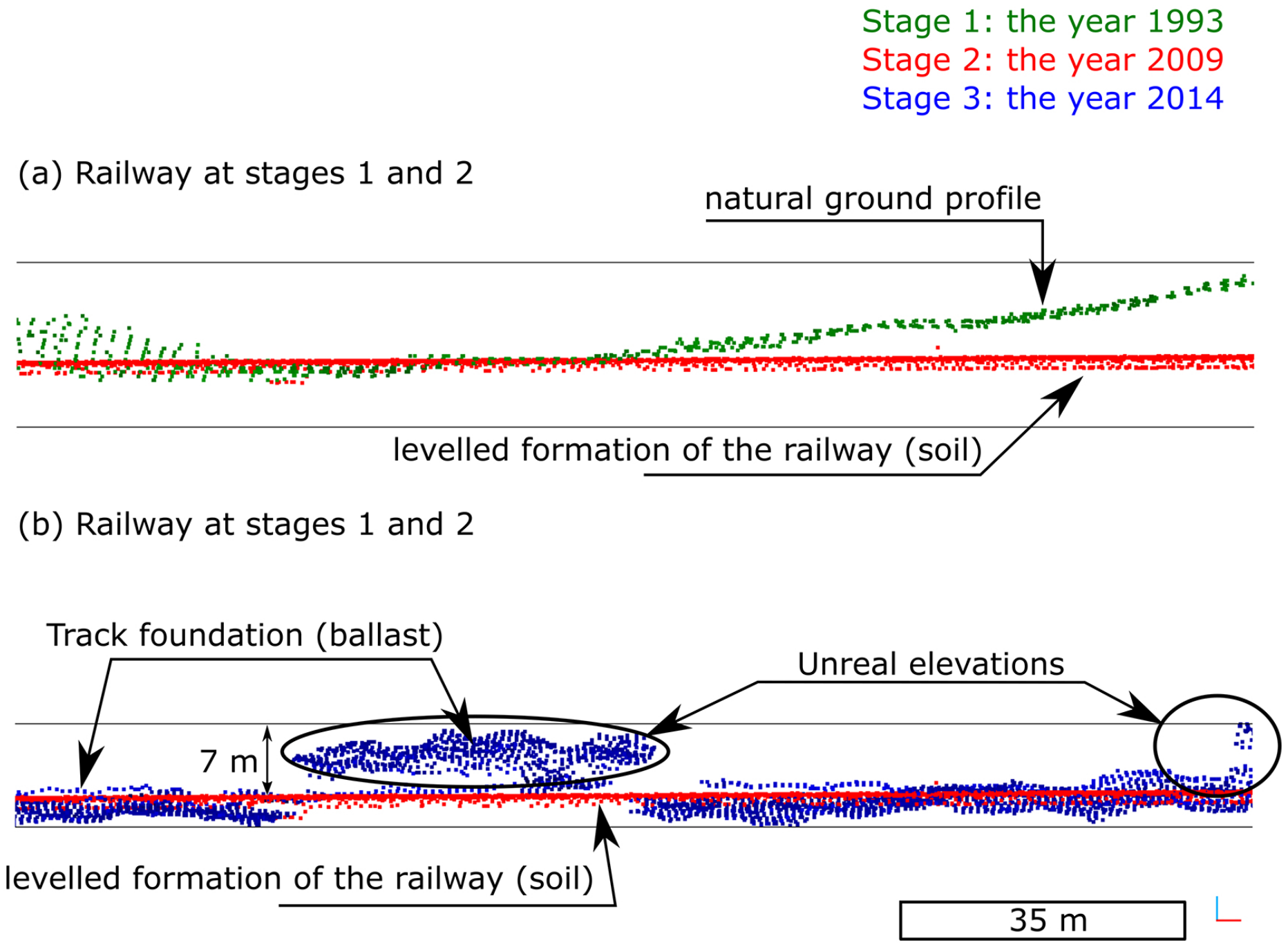
Stage 1: the year 1993
Stage 2: the year 2009
Stage 3: the year 2014
(a) Railway at stages 1 and 2
natural ground profile
levelled formation of the railway (soil)
(b) Railway at stages 1 and 2
Track foundation (ballast)
Unreal elevations
7 m
levelled formation of the railway (soil)
35 m

Figure 16